Signatures of the post-hydration heating of highly aqueously altered CM carbonaceous chondrites and implications for interpreting asteroid sample returns

Paula Lindgren [a,*], Martin R. Lee [b,*], Robert Sparkes [c], Richard C. Greenwood [d], Romy D. Hanna [e], Ian A. Franchi [d], Ashley J. King [d,f], Cameron Floyd [b], Pierre-Etienne Martin [b], Victoria E. Hamilton [g], Chris Haberle [h]

[a] *Department of Geology, Lund University, Sölvegatan 12, 223 62 Lund, Sweden*
[b] *School of Geographical & Earth Sciences, University of Glasgow, Glasgow G12 8QQ, UK*
[c] *Ecology and Environment Research Centre, Department of Natural Sciences, Manchester Metropolitan University, Oxford Road, Manchester M15 6BH, UK*
[d] *Planetary & Space Sciences, The Open University, Walton Hall, Milton Keynes MK7 6AA, UK*
[e] *Jackson School of Geosciences, The University of Texas at Austin, 2305 Speedway Stop C1160, Austin, TX 78712-1696, USA*
[f] *Department of Earth Sciences, Natural History Museum, Cromwell Road, London SW7 5BD, UK*
[g] *Southwest Research Institute, 1050 Walnut St., Suite 300, Boulder, CO 80302, USA*
[h] *School of Earth and Space Exploration, Arizona State University, Tempe, AZ 85287, USA*

Abstract

The CM carbonaceous chondrites have all been aqueously altered, and some of them were subsequently heated in a parent body environment. Here we have sought to understand the impact of short duration heating on a highly aqueously altered CM through laboratory experiments on Allan Hills (ALH) 83100. Unheated ALH 83100 contains 83 volume per cent serpentine within the fine-grained matrix and altered chondrules. The matrix also hosts grains of calcite and dolomite, which are often intergrown with tochilinite, Fe(Ni) sulphides (pyrrhotite, pentlandite), magnetite and organic matter. Some of the magnetite formed by replacement of Fe(Ni) sulphides that were accreted from the nebula. Laboratory heating to 400 °C has caused partial dehydroxylation of serpentine and loss of isotopically light oxygen leading to an increase in bulk $\delta^{18}O$ and fall in $\Delta^{17}O$. Tochilinite has decomposed to magnetite, whereas carbonates have remained unaltered. With regards to infrared spectroscopy (4000–400 cm^{-1}; 2.5–25 μm), heating to 400 °C has resulted in decreased emissivity (increased reflectance), a sharper and more symmetric OH band at 3684 cm^{-1} (2.71 μm), a broadening of the Si—O stretching band together with movement of its minimum to longer wavenumbers, and a decreasing depth of the Mg—OH band (625 cm^{-1}; 16 μm). The Si—O bending band is unmodified by mild heating. With heating to 800 °C the serpentine has fully dehydroxylated and recrystallized to ~Fo$_{60/70}$ olivine. Bulk $\delta^{18}O$ has further increased and $\Delta^{17}O$ decreased. Troilite and pyrrhotite have formed, and recrystallization of pentlandite has produced Fe,Ni metal. Calcite and dolomite were calcined at ~700 °C and in their place is an un-named Ca-Fe oxysulphide. Heating changes the structural order of organic matter so that Raman spectroscopy of carbon in the 800 °C sample shows an increased (D1 + D4) proportional area parameter. The infrared spectrum of the 800 °C sample confirms the abundance of Fe-bearing olivine and is very similar to the spectrum of naturally heated stage IV CM Pecora Escarpment 02010. The temperature-related mineralogical, chemical, isotopic and spectroscopic signatures defined

---

* Corresponding authors.
  E-mail address: Martin.Lee@Glasgow.ac.uk (M.R. Lee).

in ALH 83100 will help to track the post-hydration thermal histories of carbonaceous chondrite meteorites, and samples returned from the primitive asteroids Ryugu and Bennu.

1. INTRODUCTION

The Mighei-like (CM) carbonaceous chondrites are primitive meteorites derived from one or more parent bodies, probably C-type asteroids from the outer part of the main asteroid belt (Chapman et al., 1975; Gradie and Tedesco, 1982; Hiroi and Vilas, 1995; Lee et al., 2019a; Greenwood et al., 2020). The CMs formed by accretion of material including crystalline and amorphous silicates, oxides, metal, sulphides, organic matter and ices. These meteorites therefore provide valuable insights into the composition of the protoplanetary disk (Grossman, 1972; Wilkening, 1978). The CMs also host a suite of 'secondary' minerals including phyllosilicates, sulphides, carbonates and oxides (McSween, 1979; Bunch and Chang, 1980; Barber, 1981; Zolensky and McSween, 1988; Zolensky et al., 1993, 1997; Brearley, 2006). Whilst it has been suggested that the phyllosilicates could have formed within the solar nebula or a precursor parent body (Metzler et al., 1992; Ciesla et al., 2003), most workers conclude that the secondary minerals were all produced by aqueous alteration in the interior of the meteorite's parent body. Alteration took place within a few million years of parent body accretion (de Leuw et al., 2009; Lee et al., 2012; Fujiya et al., 2012) with the liquid water responsible being generated by melting of H_2O-rich ices in response to the decay of short-lived radionuclides (e.g., ^{26}Al; Grimm and McSween, 1989), and possibly also impacts (Rubin, 2012). The CMs have been aqueously altered to different degrees, ranging from partial to near-complete, although no unaltered (i.e., CM3) meteorites have yet been described (McSween, 1979; Browning et al., 1996; Rubin et al., 2007; Howard et al., 2009, 2011, 2015; Alexander et al., 2013).

In addition to the heating that drove aqueous alteration, at least 20 CMs have evidence for post-hydration heating (Akai, 1988; Ikeda, 1992; Tonui et al., 2014). These meteorites can be classified according to maximum temperatures reached, ranging from <250 °C to ≥750 °C (Nakamura, 2005; Tonui et al., 2014). The most prominent effects of post-hydration heating were dehydroxylation, dehydration, calcination and recrystallization of the aqueous alteration products (e.g., Nakamura, 2005, 2006; Tonui et al., 2014; Lee et al., 2016). As an example, post-hydration heating of Elephant Moraine (EET) 96029 to ~400–600 °C caused the dehydroxylation and amorphisation of serpentine, replacement of tochilinite by magnetite and loss of sulphur from the matrix; the structure of organic matter was also modified (Lee et al., 2016). It is possible that this post-hydration heating was a widespread and continuous phenomenon, with the CMs reaching a range of peak temperatures (Lee et al., 2018, 2019b), although lower temperature effects would be difficult to recognise using conventional petrographic, mineralogical or geochemical tools. Three drivers of thermal processing have been proposed, namely the decay of short-lived radionuclides (principally ^{26}Al), impacts, and solar radiative heating (Akai, 1988; Nakamura, 2005; Nakato et al., 2008). These three processes differ in the timescale and length scale of heating. ^{26}Al heating would have taken place early in solar system history, been widespread within the parent body and relatively long-lived. By contrast, radiative and impact heating would have been much shorter in duration; the former may have been relatively recent whereas the latter could have taken place at any time in solar system history. Radiative heating would have affected only the outermost parts of the parent body (e.g., temperatures of 550 K or more at <~2 m beneath the surface of a carbonaceous asteroid whilst at perihelion), with shock effects penetrating deeper beneath the surface (Chaumard et al., 2012; Wakita and Genda, 2019). A recent isotopic study of several CMs indicates that heating took place at least 3 Ga after solar system formation, thus discounting ^{26}Al as an agent (Amsellem et al., 2020). As one of these meteorites also has a heating age that is inconsistent with solar irradiation, Amsellem et al. (2020) favour the impact-heating model.

Enhancing our understanding of the processes and products of post-hydration heating is important in the context of current missions to return samples of carbonaceous asteroids (Lee et al., 2016; King et al., 2017). For example, infra-red (IR) spectroscopy results from the Cb-type asteroid (162173) Ryugu, which is being studied by the JAXA Hayabusa2 mission, may be explained by a CM2-like mineralogy that had undergone static or shock heating and thermal alteration (Perna et al., 2017; Kitazato et al., 2019). The near-Earth B-type asteroid (101955) Bennu that is the target of the NASA OSIRIS REx mission has spectral properties that are consistent with CIs and highly aqueously altered CMs that may or may not have been heated (Clark et al., 2011; Hamilton et al., 2019; Hanna et al., 2019a). Therefore, a better understanding of the nature and evolution of CM meteorites that have been both aqueously altered and heated will help considerably in the interpretation of results from these missions.

Here we describe the petrology and mineralogy, chemical and isotopic composition, and the spectroscopic properties of the CM carbonaceous chondrite Allan Hills (ALH) 83100, and document changes with laboratory heating. ALH 83100 was used as it has been highly aqueously altered (Zolensky et al., 1997; Howard et al., 2015) so that results are relevant to both Ryugu and Bennu (Le Corre et al., 2018; Hamilton et al., 2019; Hanna et al., 2019a). It is also a good starting material for laboratory heating experiments since it has not experienced (any significant) natural post-hydration heating (Alexander et al., 2013;

Quirico et al., 2018). One of the specific goals of the present study is to define the properties of a highly aqueously altered CM that are diagnostic of heating to specific temperatures so that the thermal histories of these asteroids and their constituents can be reconstructed. An understanding of how the IR spectral signature of ALH 83100 evolves as a function of heating will also help to better interpret spectral data from these small bodies and other CM-like asteroids.

2. MATERIALS AND METHODS

ALH 83100 was collected in Antarctica in 1983. It has a mass of 3.02 kg, a weathering grade of Be, and is paired with 20 other finds (Grossman, 1994). This study used a 5.755 g piece (ALH 83100,276) that was provided by ANSMET. It was divided into subsamples that were left unheated or were heated in the laboratory (Table 1). These experiments were designed to simulate short-period heating, as for example would accompany an impact into the parent body or solar heating of a rotating body close to perihelion. Subsamples in the form of chips and powders were placed in platinum crucibles then heated in a tube furnace under vacuum ($\sim 5 \times 10^3$ mbar) for 24 h. Two chips (244 mg) and a powder (43 mg) were heated to 400 °C, and two chips (234 mg) and a powder (34 mg) were heated to 800 °C. Using the classification of Nakamura (2005) these temperatures correspond to meteorite heating stages II (300–500 °C) and IV (>750 °C), respectively. Unheated and heated samples were studied by SEM, Raman spectroscopy, IR spectroscopy, oxygen isotopic analysis and X-ray diffraction (XRD) (Table 1).

Two unheated chips and three heated chips were encapsulated in resin and polished for SEM. All of them were polished using water apart from one of the chips that had been heated to 800 °C, which was polished without water in order to preserve highly soluble minerals potentially present (e.g., oldhamite) (Table 1). SEM work was undertaken at the University of Glasgow (UoG) using a Zeiss Sigma SEM equipped with an Oxford Instruments X-Max energy dispersive X-ray (EDX) spectrometer connected to Oxford Instruments INCA and AZtec software. The SEM was operated at 20 kV/$\sim$3 nA and was used for backscattered electron (BSE) imaging, qualitative and quantitative X-ray microanalysis, and X-ray mapping. Analytical details are in the Appendix.

Raman spectroscopy was undertaken at the UoG using a Renishaw inVia Raman microscope that was operated with a 514 nm laser. Calibration was undertaken with respect to wavenumber using a Si standard. Laser focusing was performed through a petrographic microscope with a × 100 objective. Raman was used to identify minerals, principally magnetite and tochilinite, and to determine the structure of carbon. Mineral identification was undertaken on the polished samples whereas organic matter analyses used powered samples; they had not received any additional treatment so that both soluble and insoluble organic matter were present. Details of Raman analysis of the organic matter are described in the Appendix.

IR spectroscopy was undertaken at the Southwest Research Institute in Boulder, Colorado. We collected reflectance spectra on thin sections rather than powders because the latter display spectral variations due to small particles ($<\sim$65–75 µm), referred to as transparency features, which to date have not been found to contribute strongly to Bennu's spectra (Hamilton et al., 2019). More importantly, meteorite powders require heating to drive off terrestrial adsorbed water that is introduced during the powdering process (e.g. Beck et al., 2010; Takir et al., 2013; Takir et al., 2019) and therefore may complicate our efforts to distinguish spectral differences among unheated and heated samples, especially in the high wavenumber region (4000–2500 cm^{-1}; 2.5–4 µm) that probes molecular water and hydroxyl. Reflectance spectra (4000–400 cm^{-1}, 2.5–25 µm) were acquired on thin sections (polished with water) using a Thermo Scientific iN10 FTIR microscope (µ-FTIR) equipped with an extended range, liquid nitrogen–cooled mercury cadmium telluride (MCT) detector, and potassium bromide (KBr) beamsplitter. The instrument has a permanently aligned, 15X, 0.7 N.A. (half angle range 20–43.5°) visible/IR objective and condenser. This is a sufficiently small solid angle that our reflectance spectra do not suffer from the band broadening effects near the Christiansen feature (CF) observed in biconical systems having large solid angles that include (near-) grazing angles of incidence and collection (Hamilton, 2018). Spectra were collected as maps over each section with an individual spot size of 300 µm per pixel and an average of 256 scans with a 2 cm^{-1} spectral sampling. A polished gold plate was used as a background (collected every 15–30 min during mapping to account for atmospheric variability and/or instrument drift) to convert measured radiance to reflectance. Spectra with evidence of interference fringes or significant contributions from epoxy (Hamilton, 2018; Hanna et al., 2020) were removed from the map and remaining spectra within each map averaged to create a bulk spectrum for the unheated ($n = 25$), 400 °C ($n = 95$) and 800 °C ($n = 54$) samples. Any remaining minor epoxy signature was removed from

Table 1
Techniques used to analyse samples of ALH 83100.

	SEM	Raman	XRD	IR	O isotopes
Chips: unheated and heated, mounted in resin, polished using water	✔	✔	–	✔	–
Chip: heated to 800 °C, mounted in resin, polished without water	✔	–	–	–	–
Powders: unheated and heated	–	✔	✔	–	✔
Chips: unheated and heated, then powdered	–	–	✔	–	✔

All chips and powders were subsamples of a single 5.755 g sample that was loaned by ANSMET.

each bulk spectrum using the approach of Hamilton (2018) and Hanna et al. (2020). Spectra at <2000 cm^{-1} are plotted here as emissivity (assuming Kirchhoff's Law, $E = 1 - R$, is sufficiently applicable, where E is the emissivity and R is the reflectance; Salisbury, 1993) for better comparison to data collected with TIR instruments that measure the apparent emissivity of planetary surfaces (e.g., Christensen et al., 2018). We calculated band centers and depths using the methodology detailed in Hanna et al. (2020). We exclude analysis of the 2900 cm^{-1} (3.4 μm) region where carbonaceous chondrite organic absorptions occur because these are complicated by the C-H spectral features of the epoxy contained within meteorite sections (Hanna et al., 2020).

Oxygen isotope compositions of the unheated, 400 °C and 800 °C samples (both powders and chips) were determined at the Open University (OU) using an infrared laser-assisted fluorination system (Miller et al., 1999; Greenwood et al., 2017). The analytical procedure is described in the Appendix. Current precision for the OU system, based on repeat analyses ($n = 39$) of an obsidian internal standard, is ± 0.052‰ for δ^{17}O, ± 0.094‰ for δ^{18}O, and ± 0.017‰ for Δ^{17}O (Greenwood et al., 2018). Oxygen isotope results are reported in standard δ notation, where δ^{18}O has been calculated as: δ^{18}O $= [(^{18}$O/^{16}O)$_{sample}$/$(^{18}$O/^{16}O)$_{ref}$ $-1] \times 1000$ (‰) and similarly for δ^{17}O using the ^{17}O/^{16}O ratio, the reference being Vienna Standard Mean Ocean Water (VSMOW). For the purposes of comparison with the results of previous studies Δ^{17}O, which represents the deviation from the terrestrial fractionation line, has been calculated as: Δ^{17}O $= \delta^{17}$O $- 0.52 \times \delta^{18}$O.

XRD was undertaken at the Natural History Museum (NHM), London. Chips were powdered using an agate mortar and pestle in a clean laboratory. Mineral phases were initially identified using a PANalytical X'Pert Pro scanning X-ray diffractometer. Approximately 1 mg of each sample was mixed with a few drops of acetone and deposited as a thin smear onto a zero background silicon substrate. XRD patterns were then collected using Co Kα_1 radiation from 5 to 65° (2θ) with a step size of 0.02° and time/step of 8 seconds, giving a total measurement time of ~8 h. Mineral phases in the samples were identified using the International Centre for Diffraction Data (ICDD) database (PDF-2). Modal mineral abundances were obtained from approximately 50 mg aliquots of the chips using an INEL X-ray diffractometer with a curved 120° position sensitive detector (PSD) in a static geometry relative to the X-ray beam and sample. The samples were loaded into an aluminium sample well using the sharp edge of a spatula to ensure a high degree of randomness in grain orientations and to minimise the effects of preferred crystal alignments (Batchelder and Cressey, 1998). Cu Kα_1 radiation was selected, and the size of the X-ray beam was restricted to 0.24 × 2.00 mm and set at an incident angle of 4.2° to the flat top of the rotating sample. XRD patterns for the meteorite samples were collected for 16 h; patterns of mineral standards were acquired under the same experimental conditions for 30 min. Differences in the incident beam flux throughout the experimental run were monitored by analysing a polished block of Fe metal at the start of each day.

A profile-stripping method was used to determine the abundance of each mineral phase present in the samples typically at >1 vol.% (Cressey and Schofield, 1996; Bland et al., 2004; Howard et al., 2009). The XRD pattern of a mineral standard was scaled to the same measurement time as the ALH 83100 sample (e.g., ×32 for the 16 hour measurement). The standard pattern was then reduced in intensity until it matched the intensity in the sample diffraction pattern, at which point it was subtracted to leave a residual sample pattern. This process was repeated for each mineral standard until zero counts remained in the residual pattern and the sum of the fit factors was one. The fit factors for the mineral standards were then corrected for relative differences in X-ray absorption to give their final volume fractions in the samples, with uncertainties typically <5 vol.% (e.g., King et al., 2015a).

3. RESULTS

Unheated ALH 83100 is composed of partially to completely aqueously altered chondrules within a fine-grained phyllosilicate-rich matrix (Zolensky et al., 1997) (Fig. 1). The matrix includes grains of anhydrous silicates, carbonates (calcite and dolomite) and sulphides (pyrrhotite, pentlandite, tochilinite) (Fig. 1). The unheated and heated samples are described below with reference to their bulk properties (mineralogy, IR spectroscopy, oxygen isotopic composition), followed by the petrography, mineralogy and chemical composition of their matrices with a focus on the principal temperature-sensitive constituents: phyllosilicates, carbonates, Fe(Ni) sulphides and organic matter.

3.1. Bulk properties of ALH 83100

3.1.1. Mineralogy determined by XRD
The bulk mineralogy of unheated samples, as quantified by XRD, is consistent with previous results from ALH 83100 and other highly aqueously altered CMs (Howard et al., 2015; King et al., 2017) (Table 2, Fig. A1). The crystalline phases identified are phyllosilicates (Mg-rich serpentine, Fe-cronstedtite), olivine, enstatite, tochilinite, magnetite, calcite and Fe(Ni) sulphides (pyrrhotite, pentlandite) (Table 2, Figs. 2, A1). With respect to the phyllosilicates, XRD patterns have sharp double peaks at ~14° and ~29° that are attributed to highly crystalline, well ordered Fe-rich serpentine crystals (i.e., cronstedtite) of slightly differing compositions. Broad reflections at ~22° and ~41° are from intergrown Mg-serpentines that are finer grained and poorly crystalline. Unheated ALH 83100 has a phyllosilicate fraction of 0.90 that corresponds to a petrologic type of 1.2 on the scale of Howard et al. (2011, 2015).

Changes to bulk mineralogy following heating are summarised in Table 2 and Fig. A1. XRD patterns from the 400 °C samples are broadly similar to unheated ALH 83100 but with subtle differences. Fe-serpentine has a single peak, tochilinite is absent, the pyrrhotite peak is broader, and oldhamite was detected (but its abundance was unquantifiable) (Fig. 2). Relative to unheated samples there is a clear reduction in the intensity of the Mg-serpentine
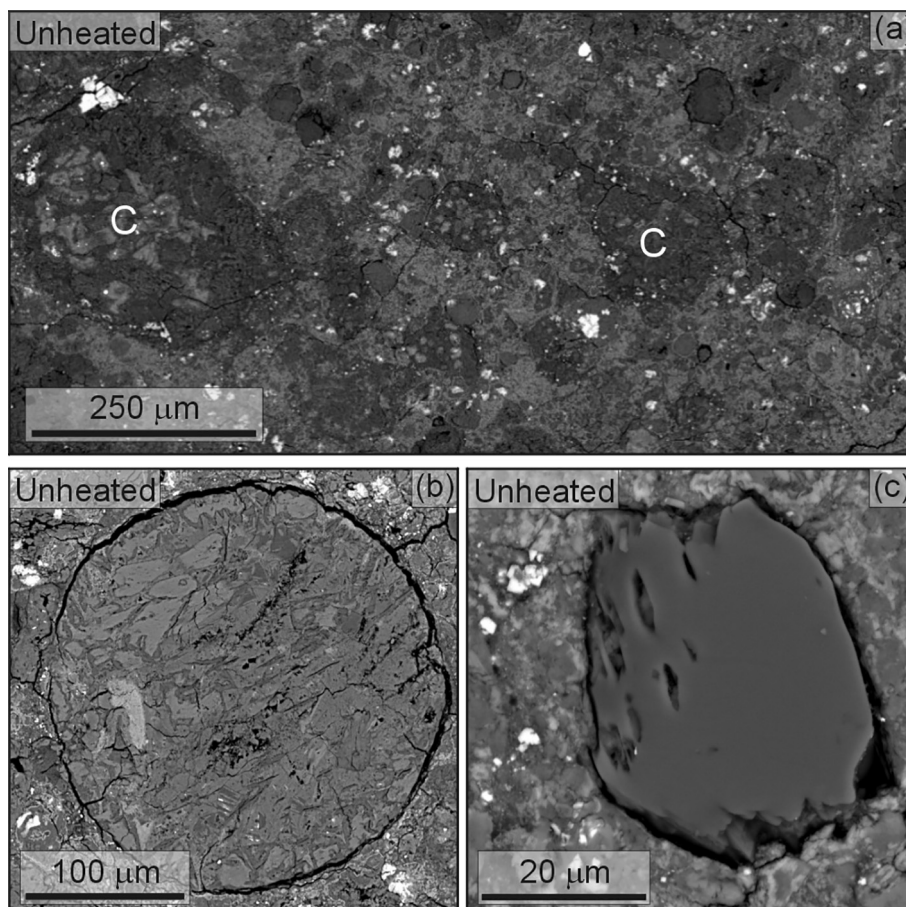
Fig. 1. BSE images of unheated ALH 83100. (a) A representative area containing chondrule pseudomorphs (C) in a fine-grained matrix with sulphides (white). (b) A chondrule pseudomorph. (c) A matrix-hosted grain of forsterite with prismatic etch pits on its left-hand side.

peak ($\sim$22°) in the powder that was heated to 400 °C but not in the chip. There is no evidence of 'amorphous scattering' that would be consistent with the presence of a highly disordered, dehydrated phyllosilicate phase. The most significant differences between the 400 °C chip and unheated ALH 83100 are 2.5 vol.% less phyllosilicate and 2.4 vol.% more Fe(Ni) sulphide (Table 2). XRD patterns of the 800 °C samples are quite distinct in containing $Fo_{60/70}$ olivine, enstatite, Fe(Ni) sulphides and Fe,Ni metal (Fig. 2, Table 2). Peaks for olivine and Fe(Ni) sulphide are more intense and broader than in the unheated and 400 °C samples, suggesting that these minerals are fine-grained and/or poorly crystalline. The peak broadening makes detection of minor phases such as calcite and magnetite difficult, as their diffraction peaks would overlap (Table 2). In common with patterns from the 400 °C samples, there is no amorphous scattering that would otherwise indicate the presence of a highly disordered and dehydrated phyllosilicate phase.

3.1.2. IR spectroscopy

IR spectra of the unheated and 400 °C samples are similar, and typical of other highly altered (CM2.0–2.1) CM chondrites (Hanna et al., 2020) (Fig. 3a, b). The largest spectral difference between the unheated and 400 °C samples is a reduced emissivity (increased reflectance) in the latter, which can be attributed to a greater abundance of sulphides (Table 2). The position of the OH stretching band at 3684 cm^{-1} (2.71 μm) is consistent with Mg-rich serpentine (Farmer, 1974; Post and Borer, 2000; Takir et al., 2013; Hanna et al., 2020) and also changes with heating at 400 °C, becoming sharper and more symmetric (Fig. 3a). Subtle spectral changes at lower wavenumbers include a broadening of the Si—O stretching region, a shift of its emission band minimum from 973 to 991 cm^{-1} wavenumbers, a decreased depth of the Mg—OH band near 625 cm^{-1} (characteristic of Mg-bearing serpentine; Farmer, 1974), and reduced emissivity near 535 cm^{-1}. The Si—O bending band appears unmodified by mild heating (Fig. 3b). Overall, both the unheated and 400 °C samples are similar to a pure Mg-Fe serpentine spectrum (Fig. 3c), consistent with their high volumetric abundances (>80 vol.%) of serpentine (Table 2). Both spectra also show very weak features that are consistent with calcite (Fig. 3c), which is notable given its low abundance as measured by XRD ($\sim$2.0 vol.%; Table 2).

The chip heated to 800 °C has an IR spectrum that is markedly different from the unheated and 400 °C samples (Fig. 3 a, b). The OH stretching band attributable to phyllosilicate is absent, and the Si—O stretching band is narrower and sharper, with minor shoulder bands that are

Table 2
Modal mineralogy of ALH 83100 determined by XRD (vol.%).

	Howard et al. (2011)	The present study		
	Unheated	Unheated	400 °C	800 °C
Mg-rich serpentine	62.4	62.0	58.1	d.l.
Fe-cronstedtite	24.2	20.8	22.2	d.l.
Olivine	8.7	5.8	4.4	88.1
Pyroxene	0.7	3.3	3.8	4.2
Pyrrhotite	n.q.	0.9	1.4	3.6
Troilite	n.q.	d.l.	d.l.	1.4
Pentlandite	n.q.	1.2	3.1	2.6
Fe,Ni metal	d.l	d.l	d.l	0.1
Magnetite	1.7	4.1	4.9	p.o.
Calcite	1.2	2.0	2.2	p.o.
Total phyllosilicate	86.6	82.8	80.3	d.l.
Total anhydrous silicates	9.4	9.1	8.2	92.3
Total Fe(Ni) sulphide	1.0	2.1	4.5	7.6
Phyllosilicate fraction (PF)	0.90	0.90	0.91	–
Petrologic type	1.2	1.2	1.2	–

Data are from chips that were heated and then powdered.
Measurement uncertainties are typically <5 vol.%.
Tochilinite is not quantified owing to the lack of a XRD standard.
d.l. – Below detection limits of ~1 vol.%.
p.o. – Peak not identified either due to its absence or overlap with a stronger silicate peak.
n.q. – Abundances of the three Fe(Ni) sulphide minerals (pyrrhotite, troilite, pentlandite) were not individually quantified by Howard et al. (2011).
PF – Total phyllosilicate/(total anhydrous silicate + total phyllosilicate).
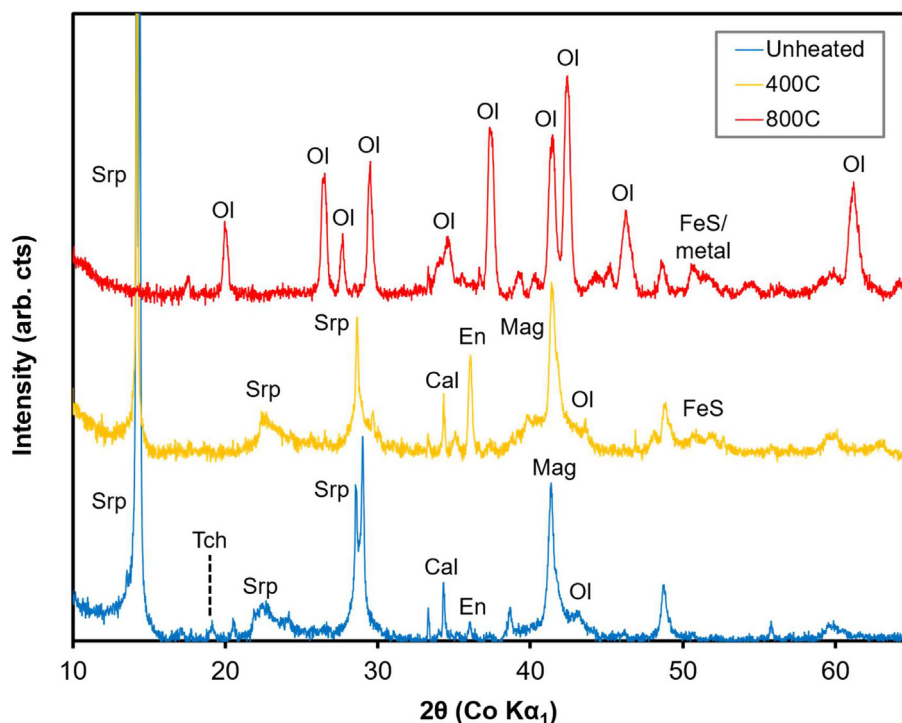

Fig. 2. XRD patterns of unheated and heated ALH 83100 collected using a PANalytical X'Pert Pro scanning XRD. Only patterns from the samples that were heated as chips then powdered are shown. Srp = serpentine; Mag = magnetite; Cal = calcite; Ol = olivine; En = enstatite; Tch = tochilinite.

indicative of Fe-bearing olivine (Fig. 3d) (Duke and Stephens, 1964; Hamilton, 2000, 2010). The Mg—OH band has disappeared, and the Si—O bending band has shifted to a lower wavenumber; the observed low-wavenumber spectral features are consistent with Fe-bearing olivine (Fig. 3d). The spectrum shows a further decrease in
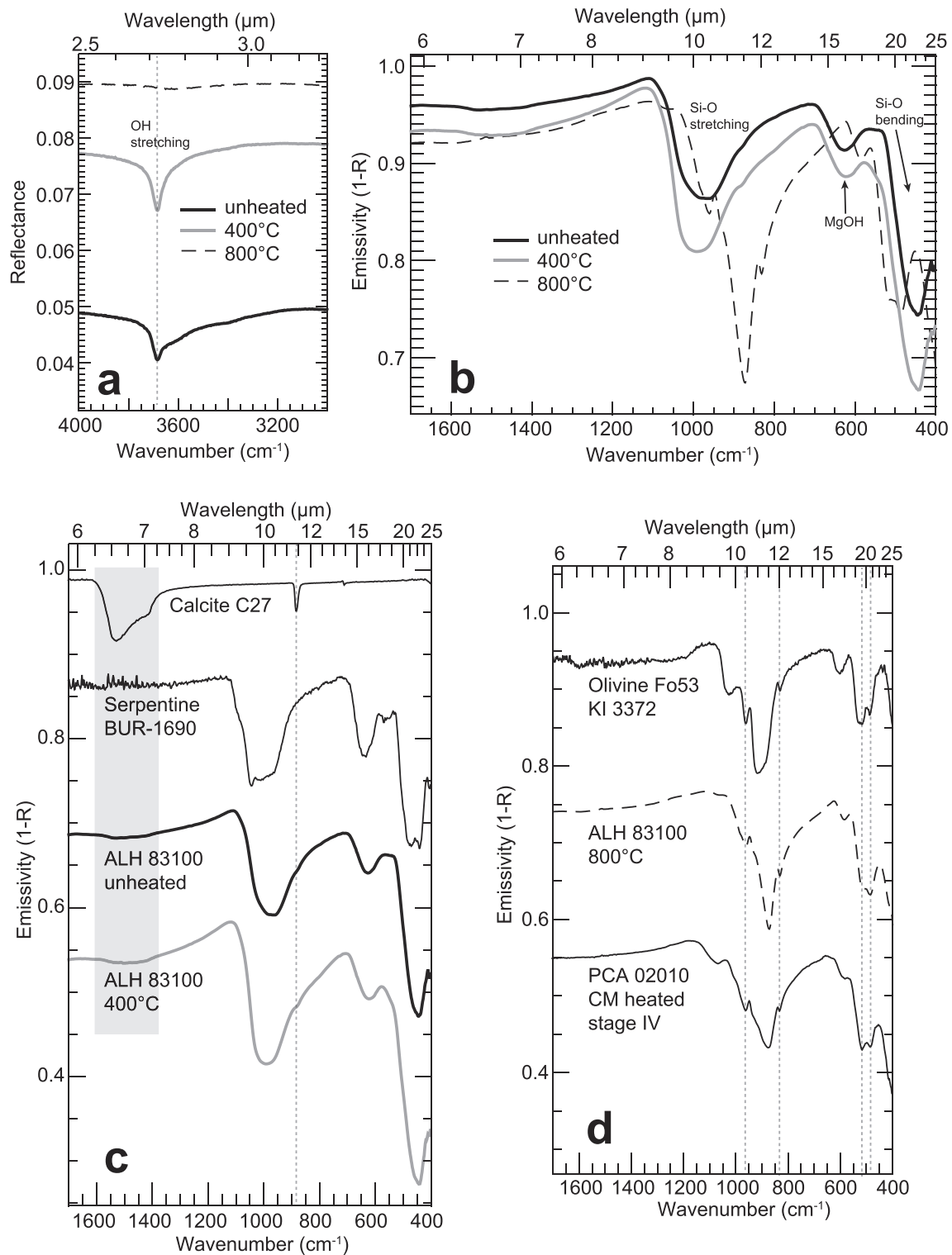
Fig. 3. (a and b) IR spectra of unheated and heated chips in thin section. Spectra are not offset or scaled. Vertical dotted line in (a) marks the OH band emission maximum (reflectance minimum) at 3684 cm^{-1} (2.71 μm) (c) The spectral shapes of both the unheated and 400° chips are similar to the emission spectrum of FeMg serpentine, with weak spectral features consistent with calcite. (d) The 800° chip shows spectral features consistent with Fe-bearing olivine, and is also similar to the spectrum of naturally heated (stage IV) CM PCA 02010 (from Hanna et al., 2020). Spectra in (c) and (d) scaled and offset for clarity and vertical dotted lines indicate spectral features due to calcite (c) and Fe-bearing olivine (d).

emissivity (increase in reflectance) at wavenumbers $>1100 \, cm^{-1}$ compared to the 400 °C sample due to increased sulphide abundance (Table 2) and a disappearance of the subtle absorption near $1500 \, cm^{-1}$ wavenumbers that was attributed to calcite in the unheated and 400 °C samples (Fig. 3b and c). In general, the IR spectrum of the 800 °C sample shows strong similarities to that of Pecora Escarpment (PCA) 02010, a strongly heated stage IV CM (on Nakamura (2005) scale, suggesting heating to ~750 °C) that is likewise dominated by secondary, Fe-bearing olivine (Beck et al., 2014a; Hanna et al., 2020).

In summary, the IR spectral results of the unheated, 400 °C, and 800 °C samples agree with the mineralogy determined by XRD and are also consistent with previously published spectra of unheated and naturally heated CM chondrites. Further, we experimentally confirm the broadening of the Si—O stretching region, weakening of the Mg—OH band, and a lack of modification of the Si—O bending band with mild heating, as found by Hanna et al. (2020) for naturally heated CMs. We also note that none of the spectra show evidence of molecular H_2O (which has significant absorptions at ~2.9–3.0 and 6 μm; Aines and Rossman, 1984), despite samples having been polished with water during preparation.

3.1.3. Oxygen isotopic composition

Results for unheated ALH 83100 are ~1‰ higher in $\delta^{17}O$ and ~1.5‰ higher in $\delta^{18}O$ than previous analyses (Table 3). However, as CM2 samples are highly heterogeneous materials and the methodology employed in earlier studies used externally heated Ni bombs (Zolensky et al., 1997; Clayton and Mayeda, 1999) such a compositional difference is not unexpected. The $\delta^{17}O$ and $\delta^{18}O$ values of powders and chips increase with heating, and together with unheated ALH 83100 the analyses plot on a line ($R^2 = 0.99$) with a slope of 0.48 (Fig. 4). The compositional changes are greater for chips than powders, especially at 800 °C.

3.2. Petrography, mineralogy and chemical composition of ALH 83100

3.2.1. Fine-grained matrix and its constituent phyllosilicates

The fine-grained matrix has a Mg-Fe silicate composition (Table 4). On a (Si + Al)-Mg-Fe ternary diagram the matrices of the unheated and 400 °C samples plot close to the serpentine solid solution line and with average atomic Mg/Fe ratios of 0.9 and 1.1, respectively. The matrix of the 800 °C sample plots close to the olivine solid solution line with an average atomic Mg/Fe ratio of 0.9 (Fig. 5a, Fig. A2a). Unheated matrix is largely composed of interlocking phyllosilicate structures that are irregular in shape and a few tens of micrometres in size thus giving a cellular appearance (Fig. 6a, b). Individual 'cells' have a ~1–2 μm wide Fe-rich rim that encloses Mg-rich phyllosilicate whose constituent crystals commonly coarsen towards its center (Fig. 6b). Phyllosilicate cells that have been heated to 400 °C are indistinguishable from those in the unheated sample. Unlike the unheated and 400 °C samples, matrix and chondrule rims of the 800 °C sample are fractured (Fig. 6c). The matrix contains features that resemble phyllosilicate cells in their size, shape, and texture, but the Fe-rich rim and Mg-rich interior are difficult to distinguish in BSE images (Fig. 6d). Plotted on a (Si + Al)-Mg-Fe ternary diagram, unheated phyllosilicate cells have a broader compositional range than those heated to 400 °C, albeit both sets of samples cluster close to the serpentine solid solution line with average Mg/Fe ratios of 2.0 and 2.1, respectively (Fig. 5b, Fig. A2b). Most analyses of cells in the 800 °C sample are compositionally distinct. They plot close to the olivine solid solution line and have a lower average Mg/Fe ratio of 0.8 (Fig. 5b, Fig. A2b).

Phyllosilicate cells in the unheated and 400 °C samples contain S-rich particles that are ~5–20 μm in size, often semicircular in shape and that stand out by virtue of their relatively high mean atomic number (Fig. 6e). SEM point counting of the unheated sample yielded a S-rich particle abundance of 1.9 vol.% ($n = 462$ points). They are composed mainly of Fe, S, Ni, Mg and Si, and are chemically similar in the unheated and 400 °C samples (Table 5). These S-rich particles are morphologically similar to polyhedral serpentine in Murchison (Lee and Lindgren, 2016) and close in composition to tochilinite in unheated CM carbonaceous chondrites (Palmer and Lauretta, 2011) (Table 5, Fig. 7). Tochilinite was identified in S-rich particles from the unheated sample by Raman spectroscopy, whereas only magnetite was detected in those particles that had been heated to 400 °C; the host of S in the 400 °C particles was not identified.

Table 3
Oxygen isotopic composition of bulk ALH 83100.

	$\delta^{17}O$‰	1σ	$\delta^{18}O$‰	1σ	$\Delta^{17}O$‰	1σ
Zolensky et al. (1997)	0.80	–	6.26	–	–	–
Clayton and Mayeda (1999)	0.82	–	6.38	–	−2.50	–
Unheated	1.943	0.179	7.848	0.238	−2.180	0.055
400 °C powder	1.994	0.002	8.275	0.028	−2.310	0.017
400 °C chip	2.240	0.061	8.737	0.108	−2.303	0.005
800 °C powder	3.068	0.129	10.942	0.268	−2.622	0.011
800 °C chip	5.868	0.027	16.170	0.045	−2.540	0.004

– Not stated.
Data from the present study are averages of two analyses.
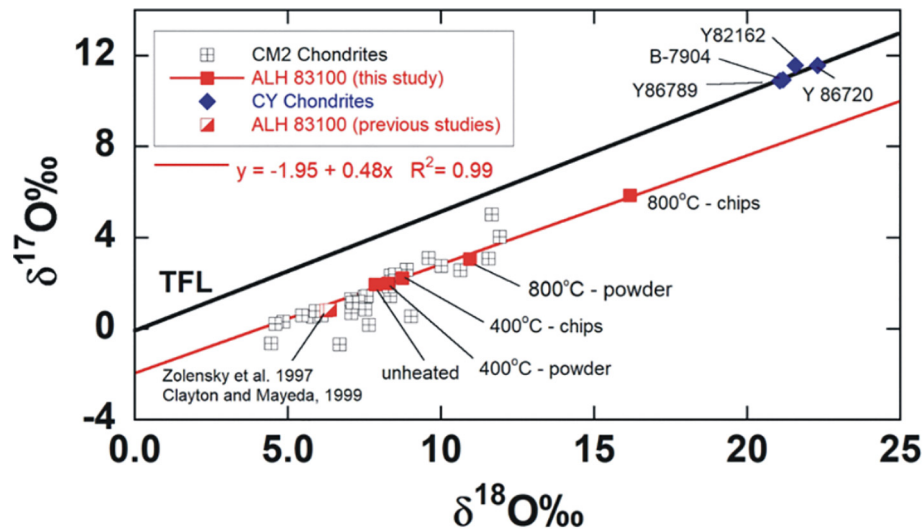1σ standard deviation.

Fig. 4. Oxygen isotopic composition of unheated and heated samples of ALH 83100 compared to previous analyses of ALH 83100 (Zolensky et al., 1997; Clayton and Mayeda, 1999) and other CM2 and CY carbonaceous chondrites (Clayton and Mayeda, 1999; King et al., 2019). A clear implication of this study is that CM2 chondrites cannot be converted into CY chondrites by heating and subsequent dehydration (see text for further discussion).

Table 4
Chemical composition of bulk ALH 83100 and its matrix (wt.%).

	Bulk[1]	Matrix[2]		
		Unheated	400 °C	800 °C
SiO_2	27.81	27.21 ± 2.46	29.99 ± 4.26	27.55 ± 2.34
TiO_2	0.11	d.l.	d.l.	d.l.
Al_2O_3	3.00	2.43 ± 0.38	2.40 ± 0.13	2.41 ± 0.41
Cr_2O_3	0.43	0.41 ± 0.06	0.23 ± 0.20	d.l.
FeO	27.24	28.26 ± 3.11	28.13 ± 8.35	36.30 ± 5.50
MnO	0.21	0.14 ± 0.17	0.03 ± 0.08	0.16 ± 0.16
MgO	18.92	14.52 ± 1.60	18.16 ± 4.77	19.35 ± 3.69
CaO	1.89	1.01 ± 0.48	0.14 ± 0.36	0.12 ± 0.14
Na_2O	0.47	0.24 ± 0.05	0.61 ± 0.19	0.40 ± 0.21
P_2O_5	0.18	0.51 ± 0.46	0.12 ± 0.27	0.03 ± 0.08
NiO	1.49	2.01 ± 0.33	1.00 ± 0.57	2.10 ± 0.63
S	1.57	1.95 ± 1.18	1.52 ± 0.68	3.29 ± 1.72
Total	83.32	78.68 ± 2.62	82.33 ± 2.47	91.70 ± 2.08
n	1	10	10	10

FeO represents iron as Fe, FeO and Fe_2O_3.
K was below detection limits in all analyses.
d.l. – below detection limits.
n – Number of analyses.
± 1σ standard deviation.
All matrix analyses are listed in the Research Data.
[1] Data from Jarosewich (1990).
[2] The matrix was analysed by SEM-EDX using a ∼10 × 10 µm raster.

3.2.2. Carbonate, sulphide and metal

The matrix of unheated ALH 83100 contains grains of calcite and dolomite that are 10–88 µm in size (average 31 µm, n = 30) (Fig. 8). These minerals have average compositions of $Ca_{0.99}Mg_{0.04}Fe_{0.07}Mn_{0.02}CO_3$ and $Ca_{1.04}Mg_{0.81}Fe_{0.10}Mn_{0.06}(CO_3)_2$, respectively (de Leuw et al., 2010), and the dolomite has previously yielded a ^{53}Mn-^{53}Cr crystallization age of $4563.9^{+0.6}_{-0.7}$ Ma (Fujiya et al., 2012). SEM shows that the two carbonate minerals also occur in the 400 °C sample, but both are absent in the sample heated to 800 °C. The unheated and 400 °C samples contain 2.0 vol.% calcite, as quantified by XRD, but dolomite could not be measured in either owing to peak overlaps with enstatite (Table 2). A previous petrographic study of a different sample of unheated ALH 83100 recorded 3.8 vol.% carbonate, comprising 1.5 vol.% calcite and 2.3 vol.% dolomite (Lee et al., 2014).

Nearly all calcite and some of the dolomite grains have a rim comprising an outer layer of Fe-rich phyllosilicate and inner layer of Mg-rich phyllosilicate. These carbonate
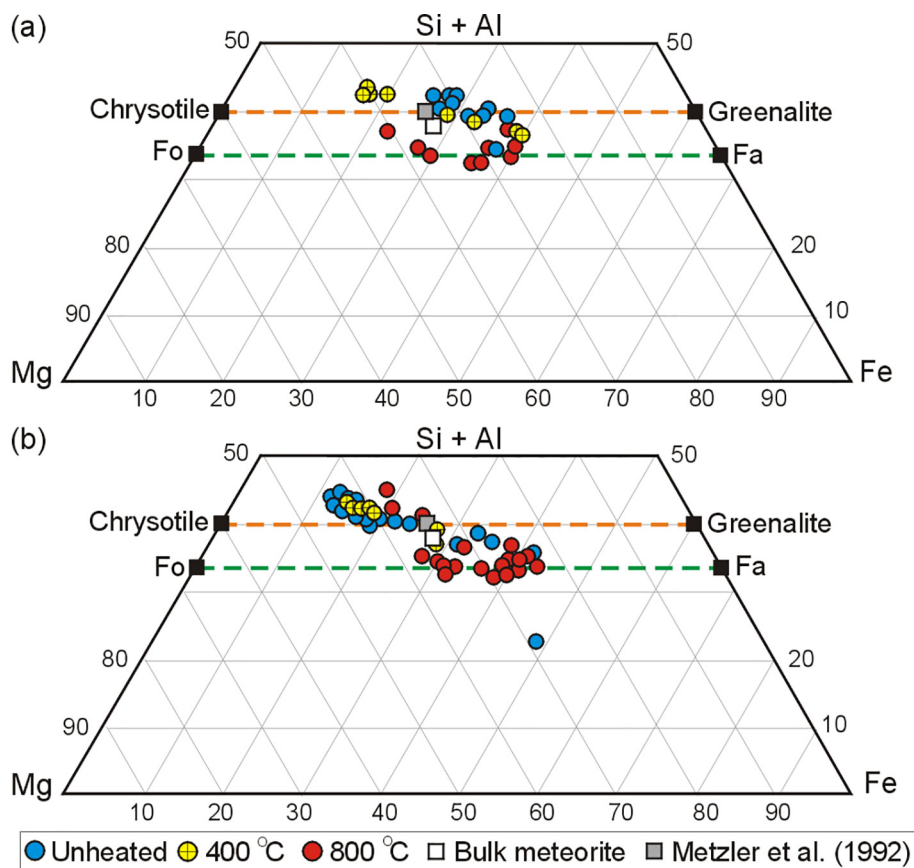
Fig. 5. Chemical composition (atomic) of unheated, 400 °C and 800 °C samples of ALH 83100. (a) The matrix. $n = 10$ analyses of each of the three samples. Compositions are listed in Table 4. (b) Phyllosilicate cells. $n = 34$, 14 and 23 analyses of the unheated, 400 °C and 800 °C samples, respectively. Compositions are listed in Table 5. Both plots include the bulk composition of unheated ALH 83100 (Jarosewich, 1990) and the average composition of fine-grained rims of unheated ALH 83100 (Metzler et al., 1992).

grains therefore occupy the centre of phyllosilicate cells (Fig. 8). Fibres of Mg-rich phyllosilicate ~1 μm in length by ~0.1 μm in width penetrate outer parts of the carbonate crystals (Fig. 8c). In the place of carbonate grains in the matrix of the 800 °C samples are Ca-rich patches tens of micrometres in size. These patches contain aggregates of ~1–3 μm size euhedral crystals containing S (~18 wt.%), Ca (~24 wt.%) and Fe (~40 wt.%) (Table 6, Figs. 9 and 10a, b); X-ray spectra show that oxygen is also present, but its abundance was not quantified. As these crystals do not match any mineral in chemical composition, they are hereafter referred to as the 'CaFeS' phase.

The volume of Fe(Ni) sulphide increases from the unheated to 400 °C and 800 °C samples (2.1, 4.5 and 7.6 vol.%, respectively; Table 2, Fig. A1). Unheated ALH 83100 contains pyrrhotite and pentlandite (Table 2), the latter stoichiometric in composition (Table A1). Grains also occur that comprise a fine-scale intergrowth of pyrrhotite with pentlandite, and one of them also has a bleb of Fe, Ni metal (Fig. 10c, d). Such grains have been classified by Singerling and Brearley (2018) as pyrrhotite-pentlandite intergrowth (PPI) grains, and micron-sized metal inclusion-bearing pyrrhotite-pentlandite intergrowth grains

(MMI-PPI), respectively. The 400 °C sample contains grains of pyrrhotite and pentlandite, the latter ranging in composition from Ni-poor ($\sim Fe_5Ni_4S_8$) to Ni-rich ($\sim Fe_4Ni_5S_8$) (Table A1). The abundance of pyrrhotite increases from 1.4 to 3.5 vol.% between the 400 °C and 800 °C samples, and in the latter is accompanied by troilite (Table 2). Analysed pentlandite grains in the 800 °C samples are Ni-poor ($\sim Fe_5Ni_4S_8$ to $Fe_{5.5}Ni_{3.5}S_8$) and contain inclusions of Fe,Ni metal ($\sim Ni_{0.67}Fe_{0.33}$) (Table A1). The FeS grains analysed in ALH 83100 are stoichiometric troilite (Table A1). P-rich sulphides were analysed only in the sample heated to 400 °C and their composition is comparable to P-rich sulphide in unheated ALH 83100 (Nazarov et al., 2009) (Table 6).

Magnetite was identified in unheated ALH 83100 by XRD, Raman spectroscopy and quantitative EDX. It occurs as monomineralic grains, and is also intergrown with Fe(Ni) sulphides, including both the PPI and MMI-PPI grain types (Fig. 10c-e). The presence of magnetite at grain edges, and cross-cutting grain interiors indicates that it has formed by replacement of the sulphide. Magnetite is also present in the 400 °C samples, and in a similar abundance to unheated ALH 83100 (4.9 vol.% and 4.1 vol.%, respec-
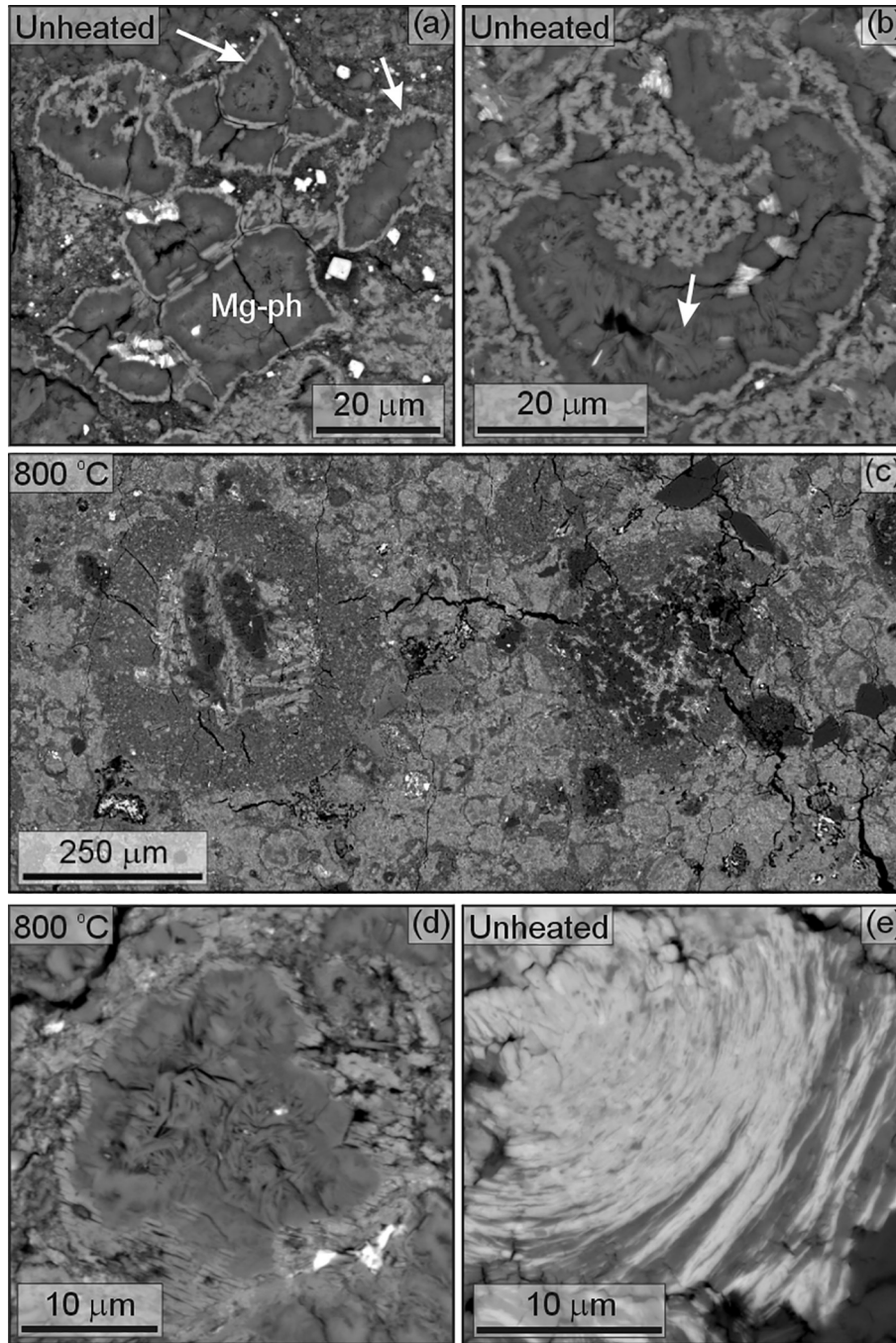
Fig. 6. BSE images of ALH 83100. (a), (b) and (e) are from the unheated sample, and (c) and (d) were heated to 800 °C. (a) A group of phyllosilicate cells that share a common structure comprising a narrow outer rim of Fe-rich phyllosilicate (light grey, arrowed) enclosing a core of Mg-rich phyllosilicate (Mg-Ph). (b) A cell within which Mg-rich phyllosilicate crystals coarsen towards its centre (arrowed). (c) Overview of a sample heated to 800 °C showing two altered chondrules, both rimmed, and the intervening matrix. Fractures cut both the rims and matrix. (d) A thermally altered phyllosilicate cell. (e) A hemispherical S-rich particle within a phyllosilicate cell.

tively). It was identified in the 800 °C samples by SEM, and so its apparent absence from XRD patterns is probably due to peak overlaps with olivine (Fig. 2).

3.2.3. Organic matter

Raman spectroscopy shows that the unheated, 400 °C and 800 °C powders contain highly disordered carbon with broad first-order D and G bands superimposed on a fluorescing background of varying intensity. Automated peak fitting into five Lorentzian peaks (Sparkes et al., 2013) showed that the G band was a combination of G and D2 peaks, and the D band a combination of D1 and D4 peaks. Example fitted spectra are in Fig. A3. Relative peak areas were used to compare the importance of the G and D

Table 5
Chemical composition of constituents of ALH 8300 matrix (wt.%).

wt.%	Phyllosilicate cells			S-rich particles		Tochilinite[1]
	Unheated	400 °C	800 °C	Unheated	400 °C	
SiO$_2$	32.52 ± 4.88	34.82 ± 3.64	27.57 ± 3.14	3.27 ± 1.88	2.19 ± 1.15	2.25 ± 0.77
TiO$_2$	d.l.	d.l.	d.l.	d.l.	d.l.	n.a.
Al$_2$O$_3$	2.23 ± 0.29	2.31 ± 0.13	2.66 ± 0.41	1.23 ± 0.71	0.38 ± 0.17	1.20 ± 0.39
Cr$_2$O$_3$	0.24 ± 0.18	0.19 ± 0.22	0.13 ± 0.21	0.02 ± 0.05	d.l.	1.12 ± 0.88
FeO	19.63 ± 7.80	20.03 ± 2.93	36.82 ± 6.90	51.06 ± 3.48	57.31 ± 2.20	56.84 ± 5.92
MnO	0.01 ± 0.05	0.02 ± 0.07	0.19 ± 0.06	d.l.	d.l.	n.a.
MgO	22.72 ± 4.26	24.18 ± 3.05	17.67 ± 3.13	4.60 ± 2.19	2.48 ± 0.97	5.94 ± 1.84
CaO	0.02 ± 0.06	d.l.	0.30 ± 0.52	0.41 ± 0.34	0.15 ± 0.15	0.16 ± 0.12
Na$_2$O	0.12 ± 0.11	0.27 ± 0.15	0.48 ± 0.31	0.17 ± 0.22	0.11 ± 0.15	n.a.
P$_2$O$_5$	d.l.	0.03 ± 0.13	0.02 ± 0.08	d.l.	d.l.	0.32 ± 0.35
NiO	0.98 ± 0.32	0.61 ± 0.70	2.06 ± 0.49	9.84 ± 1.40	10.76 ± 1.53	6.12 ± 2.16
S	1.57 ± 2.04	1.15 ± 1.20	3.74 ± 1.17	21.91 ± 3.90	22.81 ± 2.64	19.60 ± 2.07
Total	80.04 ± 4.60	83.62 ± 2.54	91.64 ± 1.99	92.52 ± 5.34	96.19 ± 3.72	93.55 ± 1.96
n	34	14	23	11	11	9

n.a. – Not analysed.
d.l. – Below detection limits.
K and Ti were below detection limits in all analyses.
n – Number of analyses.
± 1σ standard deviation.
All ALH 83100 analyses are listed in the Research Data.
[1] Palmer and Lauretta (2011). Average from analyses of tochilinite in the CMs Murchison, Murray, Cold Bokkeveld and Nogoya. Data recalculated from element to oxide.
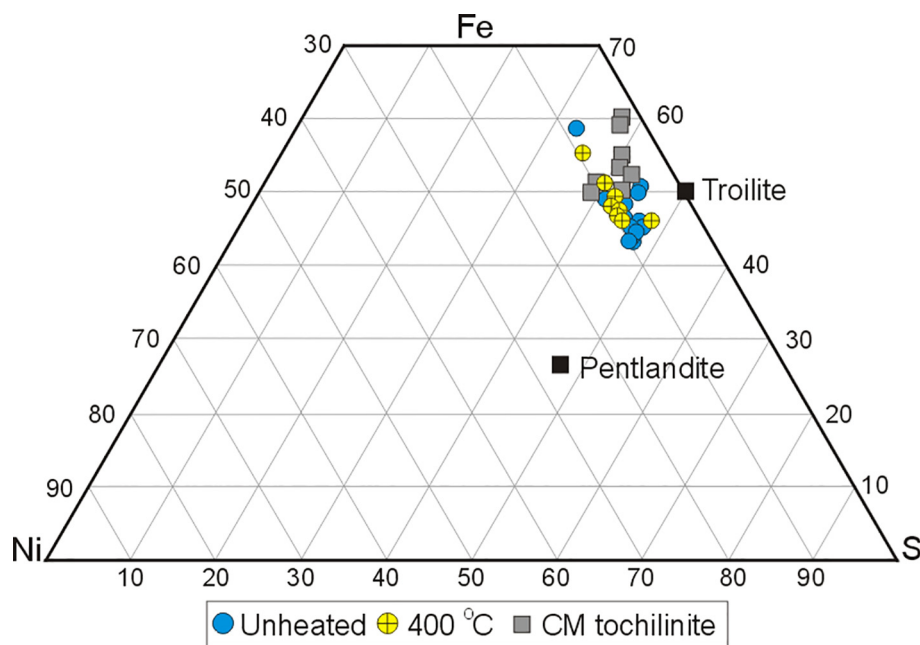

Fig. 7. Chemical composition (atomic) of S-rich particles from the unheated and 400 °C samples of ALH 83100 ($n = 11$ analyses for both) compared with tochilinite in unheated CM carbonaceous chondrites Murchison, Murray, Cold Bokkeveld and Nogoya ($n = 11$ analyses; data from Palmer and Lauretta, 2011). Average compositions of the S-rich particles and CM tochilinite are listed in Table 5. Stoichiometric pentlandite and troilite are plotted for reference.

bands, since these are more robust when dealing with bands formed from multiple peaks. Unheated and 400 °C samples had a higher relative area of G band (G + D2 peaks; 0.25c. f. 0.20), and 800 °C samples a higher relative area of the D band (D1 + D4 peaks; 0.71c.f. 0.55). The greater importance of the D band over G band is consistent with the 800 °C sample being the most thermally altered (Quirico et al., 2014, 2018).
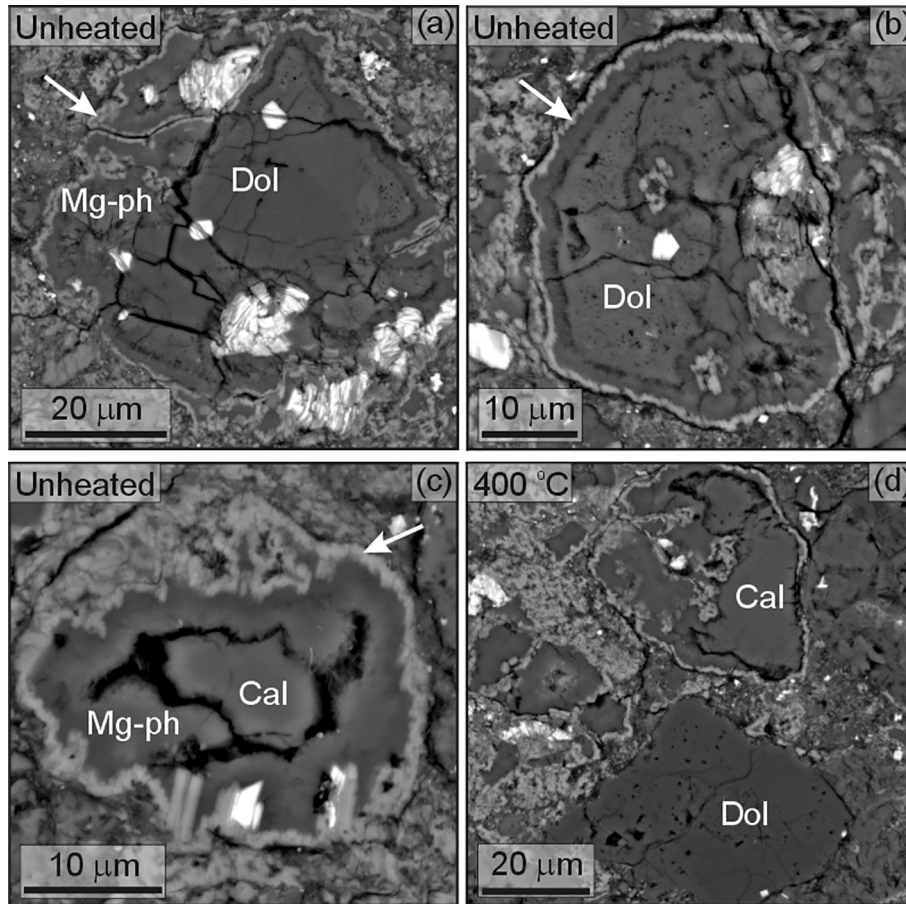
Fig. 8. BSE images of matrix-hosted grains of calcite (Cal) and dolomite (Dol). (a)–(c) are from unheated ALH 83100 and (d) is from a sample heated to 400 °C. (a) A grain of dolomite that is rimmed by an outer layer of Fe-rich phyllosilicate (light grey, arrowed) and an inner layer of Mg-rich phyllosilicate (Mg-Ph). A semicircular S-rich particle embays the lower right-hand part of the dolomite. (b) A grain of dolomite that is rimmed by an outer layer of Fe-rich phyllosilicate (arrowed) and an inner layer of Mg-rich phyllosilicate. (c) A grain of calcite that is rimmed by an outer layer of Fe-rich phyllosilicate (arrowed) and an inner layer that is Mg-rich (Mg-Ph). (d) A grain of calcite with a layered phyllosilicate rim that is adjacent to un-rimmed dolomite.

4. DISCUSSION

The aims of this study are to simulate, describe and understand the mineralogical, chemical, isotopic and spectroscopic effects of brief heating of a highly aqueously altered CM. Below we first evaluate the nature and degree of aqueous alteration of ALH 83100, then discuss how heating has affected its bulk properties, as well as the mineralogy and chemical composition of individual constituents. We then apply these results to define phases that can be used to help reconstruct the thermal evolution of carbonaceous chondrite lithologies. Finally, we summarise the implications of our results for understanding the histories of samples being returned from Ryugu and Bennu.

4.1. Degree of aqueous alteration of ALH 83100

The abundance of fine-grained matrix in unheated ALH 83100, together with the partial or complete replacement of its chondrules by phyllosilicates, indicates that it has been highly aqueously altered. Accordingly, this meteorite has a petrologic type of 1.2 on the scale of Howard et al. (2015), 1.1–1.2 as determined by Alexander et al. (2013) for ALH 83100 and four of its paired stones, and a subtype of CM2.1 (de Leuw et al., 2010). A high degree of alteration is also reflected in specific mineral properties, namely: (i) the abundance of Mg-serpentine relative to Fe-cronstedtite (3 to 1, Table 2); (ii) the scarcity of tochilinite (1.9 vol.%) and Fe,Ni metal (undetectable by XRD); (iii) relatively high volumes of magnetite (4.1 vol.%;) and carbonates (3.8 vol.% calcite plus dolomite). The mineralogy of ALH 83100 in comparison to other CMs is summarised in Fig. A1. Telus et al. (2019) used the fractionation of $\delta^{18}O$ between dolomite and magnetite to calculate that this mineral pair had crystallized at 125 °C ± 60 °C, assuming isotopic equilibrium, and this value is hereafter adopted as the temperature at which ALH 83100 was aqueously altered.

The IR spectrum of unheated ALH 83100 is also indicative of a highly altered CM. Qualitatively, its spectrum is very similar to that of other highly altered meteorites

Table 6
Chemical composition of S-rich minerals in ALH83100 (wt.%).

	CaFeS[1]	Ca,Fe oxysulphide[2]	P-rich sulphide	
			Present study 400 °C	Nazarov et al. (2009)[3]
Si	0.35 ± 0.18	0.05	1.09 ± 0.73	0.07
Cr	n.a.	<0.05	0.72 ± 0.85	d.l.
Fe	40.21 ± 1.58	42.8	36.29 ± 1.79	39.1
Mg	0.22 ± 0.18	n.a.	0.88 ± 0.61	n.a.
Ca	24.30 ± 0.86	21.4	d.l.	0.06
Na	n.a.	n.a.	0.08 ± 0.09	d.l.
P	n.a.	<0.05	1.11 ± 0.10	0.57
Ni	d.l.	0.07	17.25 ± 1.49	17.8
S	18.06 ± 1.41	20.1	32.50 ± 2.65	31.7
Total	83.04 ± 2.55[1]	84.4	89.91 ± 4.17	91.7
n	21	1	4	1

d.l. – below detection limits.
n.a. – Not analysed for.
n – Number of analyses.
± 1σ standard deviation.
All ALH 83100 analyses are listed in the Research Data.
[1] From the ALH 83100 sample that was heated to 800 °C and prepared without water. Mg was averaged from 13 analyses.
[2] Un-named phase in Dhofar 225 (Ivanova et al., 2010). Co was present at <0.05 wt.%.
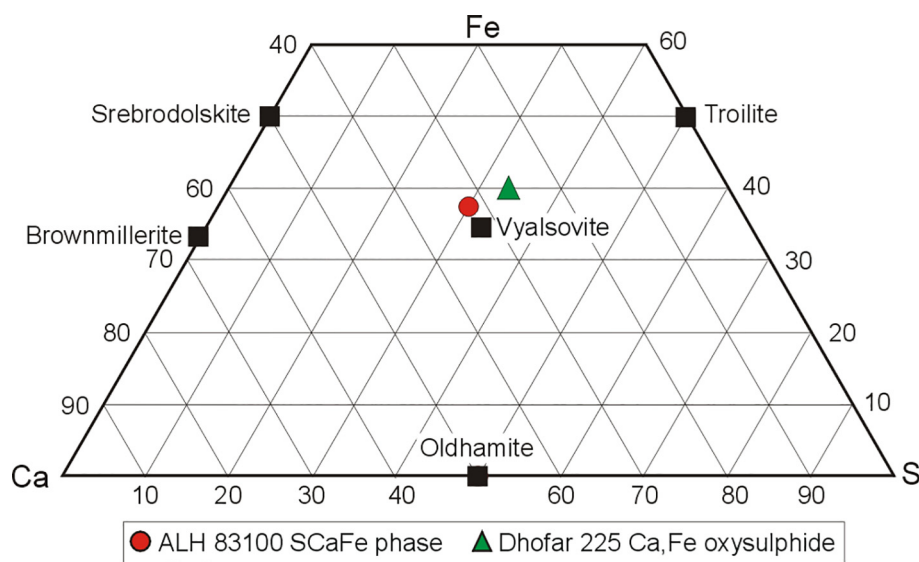[3] Includes 0.18 wt.% Co and 2.09 wt.% K.

Fig. 9. Chemical composition (atomic) of the CaFeS phase in ALH 83100 heated to 800 °C compared to Ca,Fe oxysulphide in naturally heated Dhofar 225 (Ivanova et al., 2010). Analyses of the CaFeS phase and the Ca,Fe oxysulphide are listed in Table 6. Other Ca-Fe-S minerals are plotted for reference: brownmillerite ($Ca_2(Al,Fe^{3+})_2O_5$), srebrodolskite ($Ca_2Fe_2^{3+}O_5$), vyalsovite ($Fe^{2+}SCaAl(OH)_5$), oldhamite (CaS) and troilite (FeS).

(CM2.0–2.1) (Bates et al., 2019; Hanna et al., 2020) as well as the spectrum of pure Fe-Mg serpentine (Fig. 3c). Hanna et al. (2020) found that the wavenumber distance between the Christiansen Feature (CF; maximum emissivity) and Si—O stretching band minimum was highly correlated ($R^2 = 0.90$) with petrologic subtype among a suite of unheated CMs. We calculate a petrologic subtype of CM2.0 (±0.1) for unheated ALH 83100 by using the equation defined in that work

$$y = 122.2x - 105.2$$

where x is the distance in wavenumbers between the CF (1111 cm^{-1}) and Si—O stretching band minimum (973 cm^{-1}). Thus the bulk IR spectrum of a CM thin section can be used to determine its petrologic subtype.

4.2. Thermal response of ALH 83100 components

4.2.1. Tochilinite and serpentine

Tochilinite is the most thermally sensitive mineral in ALH 83100. Estimates of its breakdown temperature range from 120 °C (Zolensky et al., 1997) to 245 °C (Fuchs et al.,
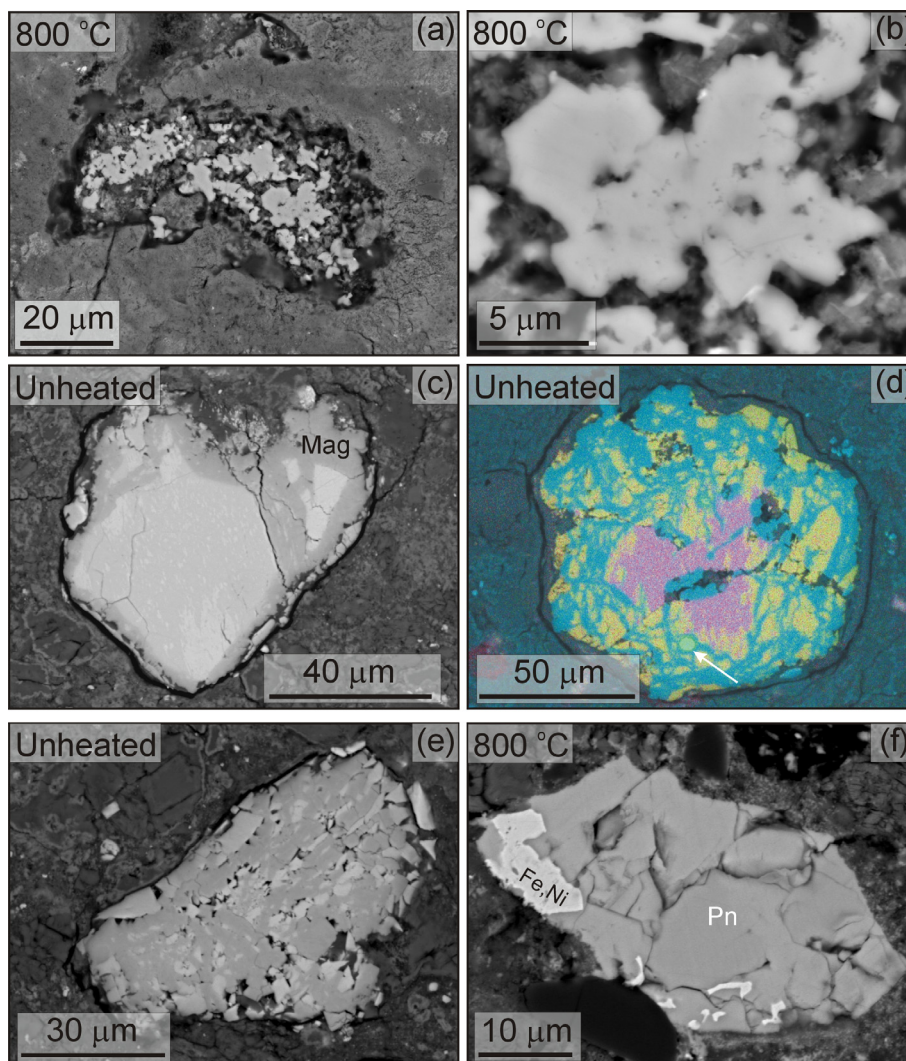
Fig. 10. Images of ALH 83100 sulphide and metal. (a), (b) and (f) are from samples heated to 800 °C, and (c), (d) and (e) are from unheated samples. (a) BSE image of a cluster of CaFeS grains (white). These grains are within a patch of porous material interpreted to be a former carbonate grain. (b) BSE image of a CaFeS grain cluster. (c) BSE image of a grain composed of a fine-scale pyrrhotite-pentlandite intergrowth (PPI) with a rim of magnetite (Mag, dark grey). (d) Multi-element X-ray map overlain on a BSE image of a grain comprising a pyrrhotite-pentlandite intergrowth with a bleb of Fe,Ni metal (MMI-PPI grain). The X-ray map is a blend of sulphur (pink), iron (light blue) and nickel (light green). This colour combination renders Fe-sulphide pink, pentlandite yellow and magnetite light blue. A small bleb of Fe,Ni metal (light green) is arrowed. (e) A sulphide grain (pentlandite/pyrrhotite) that has been extensively altered to magnetite (dark grey). (f) A grain of pentlandite (Pn) with an inclusion of Fe,Ni metal (Fe,Ni). (For interpretation of the references to colour in this figure legend, the reader is referred to the web version of this article.)

1973) and 300–400 °C (Nozaki et al., 2006). Tochilinite was identified in unheated ALH 83100 using XRD, but is absent by 400 °C, thus confirming the aforementioned breakdown temperatures. In the 400 °C sample tochilinite had decomposed to magnetite, a reaction that has also been described in experimentally heated Murchison (Tonui et al., 2014; Nozaki et al., 2006), and naturally heated EET 96029 (Lee et al., 2016). The formation of magnetite rather than troilite has been attributed to simultaneous phyllosilicate dehydroxylation raising oxygen fugacity under otherwise low fO_2 conditions (Tonui et al., 2014). It is notable that despite loss of tochilinite, the 400 °C sample contains S-

rich particles that are chemically similar to tochilinite in unheated ALH 83100 and other CMs (Fig. 7). This decoupling of the mineralogical breakdown and chemical decomposition of tochilinite was also noted in heating experiments on Murchison (Nozaki et al., 2006) (Fig. 11).

Average analytical totals for the phyllosilicate-rich matrix increase from the unheated to 400 °C and 800 °C samples (78.67 ± 2.62 wt.%, 82.32 ± 2.47 wt.% and 91.69 ± 2.08 wt.%, respectively) (Table 4). These changes are consistent with progressive thermal dehydroxylation (Velbel and Zolensky, 2019), although a range of other factors can influence analytical totals (e.g., porosity, abundance
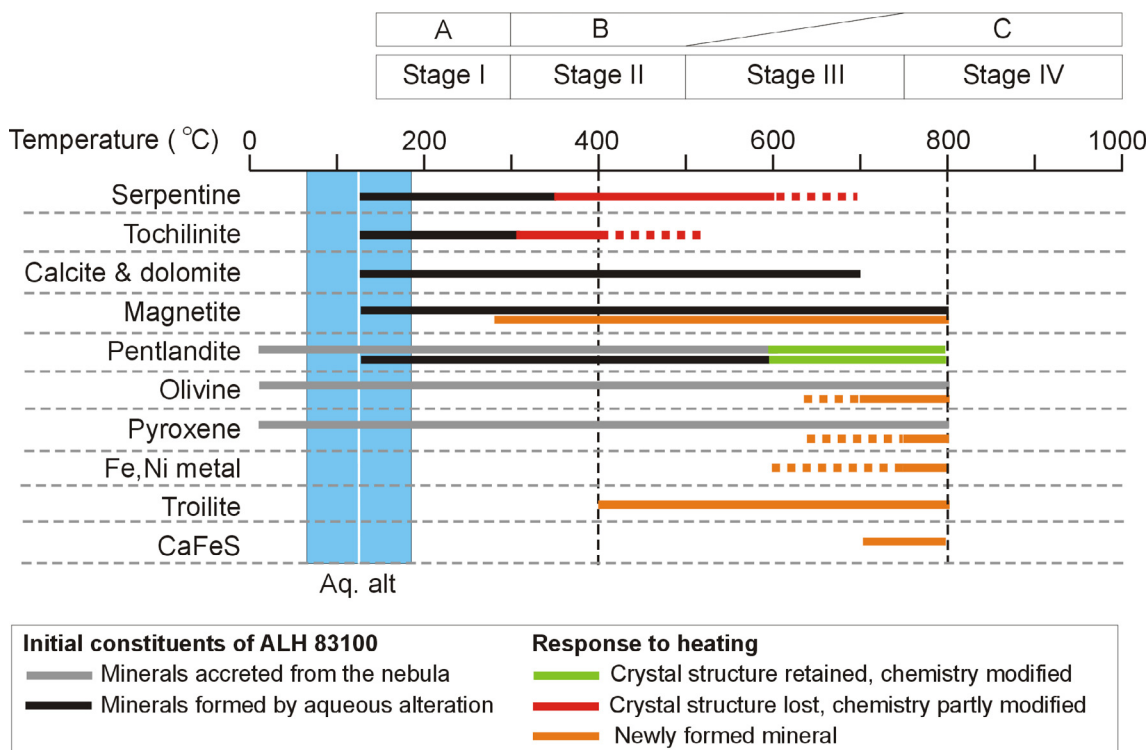
Fig. 11. Summary of the response of ALH 83100 to a short duration laboratory heating. The diagram has been constructed using results from the present study together with data from previous work as discussed in the text. The threshold temperatures of mineral formation, modification and loss may change with longer durations of heating. Laboratory temperatures are compared with two classification schemes for naturally heated carbonaceous chondrites (Stages I-IV of Nakamura, 2005; A–C of Kimura et al., 2011). The temperature of aqueous alteration of ALH 83100 (125 ± 60 °C) is indicated by the blue column (from Telus et al., 2019).

of carbon, and the proportion of anhydrous minerals in the analysed volume). The dehydroxylation and recrystallization of serpentine can also be tracked using changes to its crystal structure. XRD patterns of the unheated samples show that the main phyllosilicate peaks, at $\sim$12° and 29°, are broad and "split" into two, which may be related to slight differences in phyllosilicate composition and crystal size. The 400 °C samples lack the peak at higher angles, possibly reflecting dehydroxylation of the most Fe-rich serpentines, which break down at lower temperatures than Mg-rich serpentine (King et al., 2015b). The absence of significant amorphous scattering suggests that dehydrated 'amorphous' phyllosilicates are not a major component. In the 800 °C sample phyllosilicates are absent and have recrystallized to olivine, and possibly also pyroxene (Fig. 11). This reaction is highlighted by the abundance of olivine at 800 °C (88.1 vol.%) being almost identical to olivine plus phyllosilicate in unheated ALH 83100 (i.e., 88.6 vol.%). The chemical composition of the matrix also evolves from close to the serpentine solid solution line in the unheated and 400 °C samples, to close to the olivine solid solution line at 800 °C (Fig. 5, Fig. A2).

The start of serpentine breakdown at <400 °C is consistent with indirect measures of hydroxyl loss (i.e., matrix analytical totals, and oxygen isotopic compositions as discussed below). The modification of the OH stretching band

measured with IR spectroscopy after heating to 400 °C may also reflect the preferential breakdown of Fe-bearing serpentine as well as tochilinite, which both have shorter wavenumber absorptions ($\sim$3650–3580 cm^{-1}; $\sim$2.74–2.79 μm) compared to Mg-rich serpentine (Calvin and King, 1997; Moroz et al., 2006; Cloutis et al., 2008; Takir et al., 2013; Hanna et al., 2020;). The OH band of the unheated sample displays increased emissivity (decreased reflectance) on the short wavenumber side of its 3684 cm^{-1} (2.71) μm emissivity maximum, which is removed upon heating to 400 °C, resulting in a sharp, symmetric peak whose position is characteristic of Mg-rich serpentine. A similar sharpening of the OH band was observed when heating CM Murchison to 400 °C, which was likewise interpreted as the destruction of Fe-bearing serpentine and tochilinite (Mogi et al., 2017). By 800 °C the OH band is absent, consistent with earlier work (Hiroi et al., 1996; Mogi et al., 2017), and the serpentine has recrystallized to olivine, as evidenced by both the XRD and IR spectral results. The threshold temperature for olivine formation is likely to be slightly lower than 800 °C. Experiments on Murchison using heating steps of 100 °C showed that olivine forms at 700–800 °C (Nozaki et al., 2006), and Hiroi et al. (1993) found that Murchison serpentine had started to recrystallize to Fe-rich olivine at 600 °C. The formation of low-Ca pyroxene by the experimental heating of serpen-

tine to > 750 °C (Akai, 1992; Nakato et al., 2008) is consistent with the 0.4 vol.% increase in its abundance between 400 °C and 800 °C found in the present study (Table 2). The temperature thresholds for recrystallization of serpentine to olivine and pyroxene are summarised in Fig. 11.

4.2.2. Loss of isotopically light oxygen

Phyllosilicates are the principal host of oxygen in ALH 83100 and other highly aqueously altered CMs. Thermal dehydroxylation should modify bulk oxygen isotopic compositions through mass-dependent fractionation, leading to preferential loss of light isotopes of oxygen and enriching the bulk meteorite in heavy isotopes (Clayton and Mayeda, 1999). ALH 83100 data show that some isotopically light oxygen was lost at <400 °C, reflecting the start of dehydroxylation, with losses being more significant upon heating to 800 °C. Plotting unheated and heated samples together shows that $\delta^{17}O$ and $\delta^{18}O$ values lie on a line with a slope of 0.48 as $\delta^{18}O$ increases by a total of 8.322‰ and $\Delta^{17}O$ falls by 0.442‰ (Fig. 4). The highest $\delta^{18}O$ value was from the chip heated to 800 °C, which was considerably greater than the 800 °C powder; this result may be explained by sample heterogeneity (i.e., the chip was from an unusually phyllosilicate-rich part of the sample).

The isotopic evolution of ALH 83100 is similar to that of experimentally heated samples of the CMs Murchison and Mighei (Clayton et al., 1997; Ivanova et al., 2010) (Table A2). Ivanova et al. (2010) heated samples of Murchison to 930 °C and Mighei to 800 °C. $\delta^{18}O$ values increased by 3.77 and 3.37 ‰, and $\Delta^{17}O$ fell by 0.21‰ and 0.26‰, respectively. Results from Murchison heated over six steps (400–1000 °C) showed a smaller increase in $\delta^{18}O$ of 2.26‰, and net fall in $\Delta^{17}O$ of 0.09‰ (Clayton et al., 1997). It is notable that two aspects of the isotopic changes within these sample sets correspond with the meteorite's petrologic types (i.e., ALH 83100 = 1.2, Mighei = 1.4, Murchison = 1.5; Howard et al., 2015): (i) the magnitude of isotopic change decreases from ALH 83100 (the present study) to Murchison plus Mighei (Ivanova et al., 2010) to Murchison (Clayton et al., 1997) (Table A2); (ii) the $\Delta^{17}O$ of the regression lines increase from ALH 83100 to Mighei and Murchison (Fig. A4). The reason for these apparent correlations between thermally driven isotopic change and petrologic type is unknown. Slopes of regression lines for most of the datasets are slightly shallower than the mass-dependent terrestrial fractionation line (TFL, slope 0.52), which may be due to a contribution from organic matter to the evolved water (Mayeda and Clayton, 1998). Bulk oxygen isotopic compositions of six naturally heated CMs plot close to results from most of the heating experiments, although the 800 °C ALH 83100 chip is again significantly different (Table A2, Fig. 4). A broader implication of these results is that the CM chondrites cannot be related to the CY meteorites by any thermal process (i.e., the slope 0.5 line does not intersect the composition point for the CYs; Fig. 4).

4.2.3. Calcite and dolomite

Carbonates are petrographically comparable between the unheated and 400 °C samples whereas they are absent by 800 °C (Fig. 11). Loss of carbonates between 400 °C and 800 °C is consistent with thermogravimetric experiments on carbonaceous chondrites demonstrating decomposition by calcination at 700–900 °C (Garenne et al., 2014). Other experimental studies have provided more finely resolved decomposition temperatures. For example, Karunadasaa et al. (2019) found that the breakdown of calcite to lime (CaO) starts slowly at ∼700 °C, then proceeds rapidly above 750 °C. Valverde (2015) showed that in the presence of CO_2 dolomite decomposes to MgO and CaO at ∼700 °C. The CaO converts immediately to calcite, which itself will eventually break down at a temperature depending on the partial pressure of CO_2. Nozaki et al. (2006) found that dolomite in Murchison decomposed after experimental heating to 600 °C. Oldhamite (CaS) was identified in the 400 °C sample of ALH 83100 by XRD. This mineral can form by the calcination of calcite during natural heating of carbonaceous chondrites (Haberle and Garvie, 2017) and so it could indicate that ALH 83100 carbonates started to break down at much lower temperatures. However, as carbonates in the 400 °C sample are apparently unaltered, calcium and sulphur for the oldhamite are more likely to have been derived from the thermal decomposition of minerals such as gypsum, which occurs in Cold Bokkeveld, another highly aqueously altered CM (Lee, 1993).

Calcium-rich patches occur in the place of carbonate grains in the matrices of the 800 °C samples. Some of the calcium has been retained within the CaFeS phase (discussed below). Other hosts of calcium could be nanocrystalline lime, or Ca-pyroxene given that it is 0.4 vol.% more abundant than in the 400 °C sample (Table 2).

4.2.4. Metal and Fe(Ni) sulphide

The abundance of Fe(Ni) sulphide increases from the unheated to 400 °C and 800 °C samples (2.1, 4.5 and 7.6 vol.%, respectively), and in the IR spectra it is manifested as a progressive decrease in maximum emissivity with heating (Fig. 3). This change in sulphide abundance is mainly due to a rise in the volume of pyrrhotite, with troilite additionally present by 800 °C (Fig. 11). Whilst these mineralogical differences could reflect inter-sample heterogeneity, it is likely that temperature is responsible for the increase in the ratio of Fe-sulphide to pentlandite (i.e., 0.8–1.9 between unheated to 800 °C). The Ni/Fe ratio of pentlandite also changes with temperature. It is stoichiometric in unheated ALH 83100 (i.e., $Fe_{4.5}Ni_{4.5}S_8$), whereas grains range from Ni-poor to Ni-rich in the 400 °C sample, and are solely Ni-poor pentlandite with inclusions of Fe,Ni metal where heated to 800 °C (Table A1; Fig. 11). As pentlandite in the 400 °C sample is within the compositional range of pentlandite and intermediate sulphide in unheated CMs (Ni/(Ni + Fe) of 0.55–0.10; Chokai et al., 2004) its chemistry cannot be confidently attributed to the effects of heating. However, although pentlandite grains in the 800 °C sample are in the same compositional range, the presence of Fe,Ni metal inclusions demonstrates that their low Ni/(Ni + Fe) values are due to recrystallization.

Findings from ALH 83100 are consistent with previous studies of pentlandite stability. Terrestrial pentlandite

breaks down at 610 °C (Kullerud, 1963). In Murchison, pentlandite is unchanged by heating to 600 °C (for 1 hr and 96 hrs) but decomposes to troilite and taenite upon heating to 900 °C (Nakato et al., 2008). Temperature-related variations in the chemical composition of pentlandite in naturally heated carbonaceous chondrites were also recorded by Kimura et al. (2011). They showed that those meteorites heated to 300–750 °C contain pentlandite and intermediate sulphide whereas those heated to 500–>750 °C have only (Ni-poor) intermediate sulphide (Table A3). Therefore, Ni is lost from pentlandite upon heating to >~600 °C under both experimental and natural conditions (Fig. 11).

Fe,Ni metal was detected by XRD only in the 800 °C samples of ALH 83100, some of which will be the metal inclusions in Ni-poor pentlandite. Previous experiments confirm that Fe,Ni metal forms by heating. Experiments on Tagish Lake showed that taenite occurs at 900 °C, whereas kamacite is detectable by XRD upon heating of Murchison to 1000 °C (Tonui et al., 2014). Hiroi et al. (1993) found that Fe,Ni metal had formed at the expense of Fe,Ni sulphides by heating of Murchison to 800 °C for one week. Studies of naturally heated carbonaceous chondrites have also demonstrated high temperature generation of Ni-rich metal. Nakamura (2005) found that both kamacite and taenite were produced by natural heating to stage IV (i.e., >750 °C), and data in Kimura et al. (2011) show that Fe,Ni metal has a higher $Ni/(Ni + Fe)$ ratio in those meteorites heated to 500–>750 °C (Table A3). Thus Ni-rich Fe,Ni metal is a characteristic of both natural and experimental heating to >~600–800 °C (Fig. 11).

The CaFeS phase occurs only in samples heated to 800 °C. It is compositionally similar to an unnamed oxysulfide described from the naturally heated CM-like meteorite Dhofar 225 (Ivanova et al., 2002, 2010; Moroz et al., 2006) (Table 6). This oxysulfide occurs as small inclusions in the matrix of Dhofar 225 where it is associated with Fe,Ni metal, pyrrhotite and Fe-hydroxide. Its best-fit chemical formula is $Ca_{4.66}Fe^{2+}_{0.34}Fe^{3+}_6S_5O_9$ (Ivanova et al., 2002, 2010). Ivanova et al. (2010) suggested that the Ca,Fe oxysulphide could have formed by terrestrial oxidation of sulphide. However, the presence of the CaFeS phase within Ca-rich patches of ALH 83100 matrix suggests that it is a by-product of the calcination of calcite, with the iron and sulphur possibly coming from the breakdown of minerals including phyllosilicates and tochilinite. Such an origin would constrain the formation temperature of the CaFeS phase to between ~700 °C (the calcination threshold of calcite) and 800 °C (Fig. 11).

4.2.5. Organic matter

Heating of organic matter results in an increase in the ordering of the carbon structure, which can be shown by Raman spectroscopy (Beyssac et al., 2003). Raman analyses of carbon can reveal thermal histories of both terrestrial (Wopenka and Pasteris, 1993; Beyssac et al., 2003; Lahfid et al., 2010) and extraterrestrial samples including CM carbonaceous chondrites (Busemann et al., 2007; Beck et al., 2014b; Quirico et al., 2014, 2018). However, the modification of the carbon structure with heating in CM carbona-

ceous chondrites is not fully understood; it can take different paths depending on the duration of heating and complex interactions with minerals and fluids (Alexander et al., 2007; Quirico et al., 2018).

CM chondrites contain highly disordered carbon derived from both soluble and insoluble organic matter, and these components could have had different origins and thermal histories (Remusat et al., 2005; Quirico et al., 2014). The Raman spectra in this study were collected on bulk powders and therefore represent total organic carbon (i.e., including both the insoluble and soluble organic matter). However, the obtained spectra will mostly represent the insoluble organic matter (IOM) that is the main organic constituent; IOM makes up 70–90% of the total organic matter in carbonaceous chondrites (Sephton, 2002; Alexander et al., 2017). IOM is sensitive to relatively brief thermal events (e.g., impacts and solar heating) and so Raman spectroscopy is a powerful tool for understanding post-hydration heating of the CMs (Quirico et al., 2018). In the present study the organic matter is assumed to have been accreted, and so in the unheated sample will have been processed during accretion (e.g., by syn-accretion impacts) and during aqueous alteration. Quirico et al. (2018) classified ALH 83100 IOM in their group R1:IR1, denoting that it is chemically and structurally unmodified (R1:IR1 corresponds to heating stage I of Nakamura, 2005). This meteorite is thus good starting material for heating experiments.

Raman results show that samples heated to different temperatures can readily be distinguished in the D band vs G band diagram, after deconvolution into five constituent peaks (Fig. 12). Unheated and 400 °C samples produced similar spectra, suggesting that brief and mild heating may not be causing significant structural change in the organic matter. Quirico et al. (2018) showed that data obtained from Raman spectra of disordered carbon are not easily comparable or reproducible between laboratories, and that the analytical treatment of spectra is critical for reliable analyses. In our study, the collected Raman spectra were processed using automated fitting procedures following Sparkes et al. (2013); see the Appendix for collection and processing of Raman spectra. In Fig. 12 the data from ALH 83100 are compared with a larger database of CM chondrites from Lee et al. (2016) that were collected and treated using the same methods as in the present study. Fig. 12 shows mean and standard deviations for the (G + D2) vs. (D1 + D4) proportional areas. Naturally heated samples have higher averages for the (D1 + D4) proportional area parameter than unheated samples, but there is overlap with the unheated samples so this pattern needs closer attention in future studies. The samples heated to 800 °C have a much higher (D1 + D4) proportional area than any of the other meteorites (0.71 ± 0.09 mean ± 1 s.d. compared to means ranging from 0.47 to 0.56). This (D1 + D4) proportional area increase has also been measured in metamorphic rocks with increasing thermal alteration (Lahfid et al., 2010). These results show that carbon structure is a useful tool for understanding the nature of short duration heating of a highly aqueously altered CM, but further experimental work is needed to understand the modification of the carbon structure, as recorded by
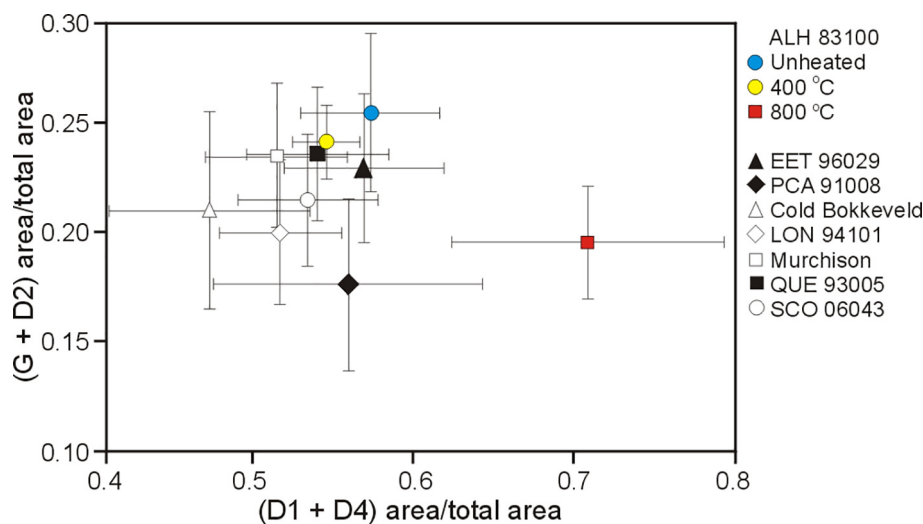
Fig. 12. Results from Raman analyses of carbon in ALH 83100. Shown is the area of the (G + D2) peaks as a proportion of total area (G, D1-4), plotted against the proportional area of (D1 + D4) peaks. Error bars are 1σ standard deviation. Plotted along with unheated and heated ALH 83100 are other CMs, both unheated (open symbols) and naturally heated (closed symbols; from Lee et al., 2016). Abbreviations of meteorite names are: EET (Elephant Moraine), PCA (Pecora Escarpment), LON (Lonewolf Nunataks), QUE (Queen Elizabeth Range), SCO (Scott Glacier). The number of spectra analysed from each sample are: ALH 83100 unheated ($n = 27$), 400 °C ($n = 38$), 800 °C ($n = 34$), EET 96029 ($n = 49$), PCA 91008 ($n = 22$), Cold Bokkeveld ($n = 45$), LON 94101 ($n = 40$), Murchison ($n = 43$), QUE 93005 ($n = 43$), SCO 06043 ($n = 40$).

Raman data, for short duration low temperature heating (i.e., 400 °C).

4.3. Implications for Ryugu and Bennu

Ryugu and Bennu both appear to be dominated by CM-type material (Le Corre et al., 2018; Hamilton et al., 2019; Kitazato et al., 2019). Based on a weak, narrow absorption at 2.72 μm observed with the Near-Infrared Spectrometer (NIRS3) on the Hayabusa2 spacecraft, Kitazato et al. (2019) interpreted Ryugu's surface to have experienced shock and/or heating. Because our IR data were collected on thin sections, which may contain a contribution from specular reflection at wavelengths <8 μm, our spectra of the OH stretching band cannot be directly compared to the spectral observations of asteroids (Hanna et al., 2020; Moroz et al., 2006). However, our spectral results confirm that while the OH band is still present at 400 °C it has lost the shorter wavenumber absorptions (~3650–3580 cm^{-1}; ~2.74–2.79 μm) attributable to Fe-bearing serpentine and tochilinite, and that at 800 °C the OH band has completely disappeared. This result suggests that Ryugu, which retains a weak band at 2.72 μm with no evidence of a longer wavelength absorption that would be due to Fe-bearing serpentine or tochilinite, has been heated to at least 400 °C but below 800 °C. If this is the case, based on our mineralogical and organics results above, we would expect the returned sample to consist of some amount of crystalline Mg serpentine, little to no crystalline Fe-rich serpentine or tochilinite, pentlandite with variable Ni compositions, possibly troilite, and the organic matter would show a higher Raman carbon (D1 + D4) proportional area parameter than unheated CM samples. This is of course a simplistic interpretation based on one

set of heating experiments that may not accurately reflect the starting material on Ryugu nor its conditions of heating (or shock), but provides tantalizing prospects of what we may find in the returned sample.

In contrast to Ryugu, Bennu has a strong OH absorption band more typical of hydrated CM and CI chondrites (Hamilton et al., 2019). Its minimum has been measured at 2.74 μm (±0.01) (Hamilton et al., 2019), which could indicate the presence of Fe-bearing serpentine but has also been interpreted to represent poorly crystalline or disordered Mg serpentine characteristic of ungrouped C2s such as Essebi and Tagish Lake (Hanna et al., 2019b). The OSIRIS-REx spacecraft is also equipped with the OSIRIS-REx Thermal Emission Spectrometer (OTES), whose measurements are directly comparable to our laboratory spectral measurements at wavelengths >~8 μm (see Hamilton (2018) and Hanna et al. (2020) for details). Based on the OTES global spectrum of Hamilton et al. (2019), Bennu may show evidence for mild heating in the form of a broadened Si—O stretching band and the absence of an Mg—OH band near 625 cm^{-1} (Fig. 13); heating of ALH 83100 to 400 °C resulted in both of these spectral modifications (although the Mg—OH band did not completely disappear). However, broadening of the Si—O stretching band on Bennu could also be explained by presence of fine particles (e.g., Salisbury et al., 1987) or space weathering (Lantz et al., 2017; Brunetto et al., 2018), although neither effect (as described in the literature) should modify or completely mask the 625 cm^{-1} Mg—OH band. We can rule out significant, widespread heating (~800 °C) on Bennu based on retention of a strong OH band and its Si—O bending band position and shape that is inconsistent with abundant Fe-bearing olivine typical of strongly heated CMs (Fig. 13). We do not preclude the possibility that localized areas
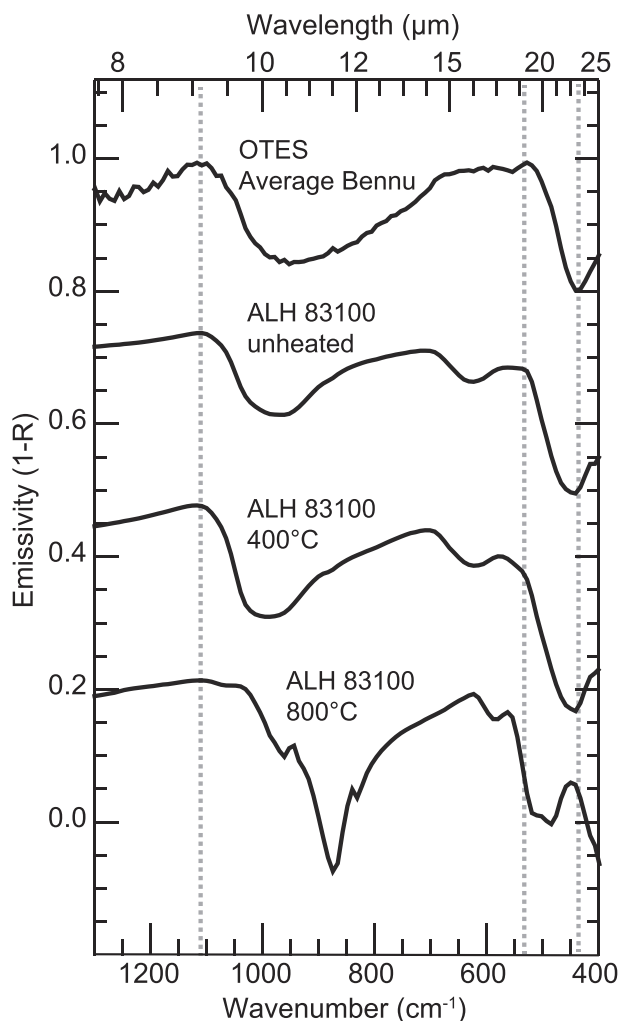
Fig. 13. Global average Bennu OTES spectrum from Hamilton et al. (2019) plotted with spectra from the present study. Spectra have been offset for clarity, and the Bennu spectrum has been scaled for comparison to the laboratory spectra. Dotted lines highlight that the CF, emissivity maximum near 530 cm^{-1} (18.9 μm), and Si—O bending minimum of the Bennu spectrum more closely match unheated or mildly heated ALH 831000, although the wider Si—O stretching band and weaker Mg—OH band of the 400 °C sample are more consistent with Bennu's spectral shape.

may show spectral evidence of significant (800 °C) heating in future higher resolution, spatially resolved OTES spectra.

Other evidence for possible heating of Bennu's surface includes thermally induced in-situ breakdown of boulders (Molaro et al., 2020), particle ejection caused by volatile release from the breakdown of hydrous minerals (Lauretta et al., 2019; Molaro et al., 2020), and spectral evidence for the presence of magnetite (Hamilton et al., 2019). The latter is commonly found in mildly heated CMs (Tonui et al., 2014), and both our experimental heating results herein and previous work on EET 96029 (Lee et al., 2016), indicate that magnetite forms at the expense of tochilinite with mild heating (<400 °C). Therefore,

although the spectral evidence for mild (400 °C) heating on Bennu is ambiguous, there are other indications for heating on Bennu, and further experiments of heating CM and possibly CI material should be undertaken.

5. CONCLUSIONS

The CM carbonaceous chondrite ALH 83100 contains minerals and organic matter that accreted from the solar nebula together with phases that formed by parent body aqueous alteration at ~125 °C. Brief laboratory heating of ALH 83100 to 800 °C has resulted in the loss of tochilinite, serpentine, calcite and dolomite, chemical and mineralogical modification of pentlandite, and alteration of organic matter (Figs. 11, A2). Carbon dioxide and OH/H_2O with isotopically light oxygen were liberated. All of the phases that formed by heating are rich in iron, and often also sulphur: olivine, pyrrhotite, troilite, Fe,Ni metal and Ca-Fe oxysulphide. The products of several reactions are useful as palaeothermometers, as diagramatically summarised in Fig. 11:

- Tochilinite crystal structure breaks down at 300–400 °C, but tochilinite-rich particles can retain their chemical composition up to and probably above 400 °C;
- The crystal structure of serpentine starts to break down at just under 400 °C. The phyllosilicate has completely dehydroxylated and transformed to nanocrystalline olivine by 800 °C;
- Isotopically light oxygen is lost preferentially during dehydroxylation, and bulk rock compositions are correspondingly enriched in isotopically heavy oxygen. Bulk meteorite compositions evolve sub-parallel to the TFL;
- Troilite and pyrrhotite form at between 400 and 800 °C;
- S, Fe and Ni are mobile within pentlandite at >610 °C. This sulphide is partially replaced by Fe,Ni metal (~$Ni_{0.67}Fe_{0.33}$) but otherwise retains its crystal structure.
- An unnamed phase that is rich in Ca, Fe and S forms at >700 °C as a by-product of the calcination of carbonates.
- More experiments are needed to understand the Raman signature of carbon during mild heating (400 °C), but at higher temperatures (800°) the structural order of carbon in CMs is a good indicator of heating, showing an increased Raman carbon (D1 + D4) proportional area parameter.
- Results from IR spectral analyses shows that at 400 °C the OH band is still present but the shorter wavenumber absorptions (~3650–3580 cm^{-1}; ~2.74–2.79 μm) characteristic of Fe-bearing serpentine and tochilinite are lost. At 800 °C the OH band has completely disappeared, and spectral features attributable to secondary, Fe-bearing olivine are apparent.

Declaration of Competing Interest

The authors declare that they have no known competing financial interests or personal relationships that could have appeared to influence the work reported in this paper.

ACKNOWLEDGEMENTS

APPENDIX A. SUPPLEMENTARY DATA

Supplementary data to this article can be found online at https://doi.org/10.1016/j.gca.2020.08.021.

REFERENCES

Aines R. D. and Rossman G. R. (1984) Water in minerals? A peak in the infrared. *J. Geophys. Res.* **89**, 4059–4071.

Akai J. (1988) Incompletely transformed serpentine-type phyllosilicates in the matrix of Antarctic CM chondrites. *Geochim. Cosmochim. Acta* **74**, 1593–1599.

Akai J. (1992) T-T–T diagram of serpentine and saponite, and estimation of metamorphic degree of Antarctic carbonaceous chondrites. *Proc Nat. Inst. Polar Res. Symp. Antarctic Meteorites* **5**, 120–135.

Alexander C. O. D., Fogel M., Yabuta H. and Cody G. D. (2007) The origin and evolution of chondrites recorded in the elemental and isotopic compositions of their macromolecular organic matter. *Geochim. Cosmochim. Acta* **71**, 4380–4403.

Alexander C. O. D., Howard K. T., Bowden R. and Fogel M. L. (2013) The classification of CM and CR chondrites using bulk H, C and N abundances and isotopic compositions. *Geochim. Cosmochim. Acta* **123**, 244–260.

Alexander C. M. O. D., Cody G. D., De Gregorio B. T., Nittler L. R. and Stroud R. M. (2017) The nature, origin and modification of insoluble organic matter in chondrites, the major source of Earth's C and N. *Chemie der Erde - Geochemistry* **77**, 227–256.

Amsellem E., Moynier F., Mahan B. and Beck P. (2020) Timing of thermal metamorphism in CM chondrites: Implications for Ryugu and Bennu future sample return. *Icarus* **339** 113593.

Barber D. J. (1981) Matrix phyllosilicates and associated minerals in C2M carbonaceous chondrites. *Geochim. Cosmochim. Acta* **45**, 945–970.

Bates H. C., King A. J., Donaldson Hanna K., Bowles N. E. and Russell S. S. (2019) Linking mineralogy and spectroscopy of highly aqueously altered CM and CI carbonaceous chondrites in preparation for primitive asteroid sample return. *Meteorit. Planet. Sci.* **55**, 77–101.

Batchelder M. and Cressey G. (1998) Rapid, accurate phase quantification of clay-bearing samples using a position-sensitive X-ray detector. *Clays Clay Minerals* **46**, 183–194.

Beck P., Quirico E., Montes-Hernandez G., Bonal L., Bollard J., Orthous-Daunay F.-R., Howard K. T., Schmitt B., Brissaud O., Deschamps F., Wunder B. and Guillot S. (2010) Hydrous mineralogy of CM and CI chondrites from infrared spectroscopy and their relationship with low albedo asteroids. *Geochim. Cosmoch. Acta* **74**, 4881–4892.

Beck P., Garenne A., Quirico E., Bonal L., Montes-Hernandez G., Moynier F. and Schmitt B. (2014a) Transmission infrared spectra (2–25μm) of carbonaceous chondrites (CI, CM, CV–CK, CR, C2 ungrouped): Mineralogy, water, and asteroidal processes. *Icarus* **229**, 263–277.

Beck P., Quirico E., Garenne A., Yin Q.-Z., Bonal L., Schmitt B., Montes-Hernandez G., Montagnac G., Chiriac R. and Toche F. (2014b) The secondary history of Sutter's Mill CM carbonaceous chondrite based on water abundance and the structure of its organic matter from two clasts. *Meteorit. Planet. Sci.* **49**, 2064–2073.

Beyssac O., Goffé B., Petitet J.-P., Froigneux E., Moreau M. and Rouzaud J.-N. (2003) On the characterization of disordered and heterogeneous carbonaceous materials using Raman spectroscopy. *Spectrochim. Acta A* **59**, 2267–2276.

Bland P. A., Cressey G. and Menzies O. N. (2004) Modal mineralogy of carbonaceous chondrites by X-ray diffraction and Mössbauer spectroscopy. *Meteorit. Planet. Sci.* **39**, 3–16.

Brearley A. J. (2006) The action of water. In *Meteorites and the Early Solar System II* (eds. D. S. Lauretta and H. Y. McSween). University of Arizona Press, pp. 587–624.

Browning L. B., McSween H. Y. and Zolensky M. E. (1996) Correlated alteration effects in CM carbonaceous chondrites. *Geochim. Cosmochim. Acta* **60**, 2621–2633.

Brunetto R., Lantz C., Dionnet Z., Borondics F., Aléon-Toppani A., Baklouti D., Barucci M. A., Binzel R. P., Djouadi Z., Kitazato K. and Pilorget C. (2018) Hyperspectral FTIR imaging of irradiated carbonaceous meteorites. *Planet. Space Sci.* **158**, 38–45.

Bunch T. E. and Chang S. (1980) Carbonaceous chondrites –II: Carbonaceous chondrite phyllosilicates and light element geochemistry as indicators of parent body processes and surface conditions. *Geochim. Cosmochim. Acta* **44**, 1543–1577.

Busemann H., Alexander C. M. O. D. and Nittler L. R. (2007) Characterization of insoluble organic matter in primitive meteorites by microRaman spectroscopy. *Meteorit. Planet. Sci.* **42**, 1387–1416.

Calvin W. M. and King T. V. V. (1997) Spectral characteristics of iron-bearing phyllosilicates: comparison to Orgueil (CI1), Murchison and Murray (CM2). *Meteorit. Planet. Sci.* **32**, 693–701.

Chapman C. R., Morrison D. and Zellner B. (1975) Surface properties of asteroids using a synthesis of polarimetry, radiometry and pectrophotometry. *Icarus* **25**, 104–130.

Chaumard N., Devouard B., Delbo M., Provost A. and Zanda B. (2012) Radiative heating of carbonaceous near-Earth objects as a cause of thermal metamorphism for CK chondrites. *Icarus* **220**, 65–73.

Chokai J., Zolensky M., Le L., Nakamura K., Mikouchi T., Monkawa A., Koizumi E. and Miyamoto M. (2004) Aqueous alteration mineralogy in CM carbonaceous chondrites. *Lunar Planet. Sci.* **XXXV**, #1506 (abstr.).

Christensen P. R., Hamilton V. E., Mehall G. L., Pelham D., O'Donnell W., Anwar S., Bowles H., Chase S., Fahlgren J., Farkas Z., Fisher T., James O., Kubik I., Lazbin I., Miner M., Rassas M., Schulze L., Shamordola K., Tourville T., West G., Woodward R. and Lauretta D. (2018) The OSIRIS-REx

Thermal Emission Spectrometer (OTES) Instrument. *Space Sci. Rev.* **214**, 87.

Ciesla F. J., Lauretta D. S., Cohen B. A. and Hood L. L. (2003) A nebular origin for chondritic fine-grained phyllosilicates. *Science* **299**, 549–552.

Clark B. E., Binzel R. P., Howell E. S., Cloutis E. A., Ockert-Bell M., Christensen P., Barucci M. A., DeMeo F., Lauretta D. S., Connolly H., Soderberg A., Hergenrother C., Lim L., Emery J. and Mueller M. (2011) Asteroid (101955) 1999 RQ36: Spectroscopy from 0.4 to 2.4 um and meteorite analogs. *Icarus* **216**, 462–475.

Clayton R. N., Mayeda T. K., Hiroi T., Zolensky M. and Lipschutz M. E. (1997) Oxygen isotopes in laboratory heated CI and CM chondrites (abstract). *Meteorit. Planet. Sci.* **32**, A30.

Clayton R. N. and Mayeda T. K. (1999) Oxygen isotope studies of carbonaceous chondrites. *Geochim. Cosmochim. Acta* **63**, 2089–2104.

Cloutis E. A., Craig M. A., Kruzelecky R. V., Jamroz W. R., Scott A., Hawthorne F. C. and Mertzman S. A. (2008) Spectral reflectance properties of minerals exposed to simulated Mars surface conditions. *Icarus* **195**, 140–168.

Cressey G. and Schofield P. F. (1996) Rapid whole-pattern profile stripping method for the quantification of multiphase samples. *Powder Diffr.* **11**, 35–39.

de Leuw S., Rubin A. E., Schmitt A. K. and Wasson J. T. (2009) ^{53}Mn-^{53}Cr systematics of carbonates in CM chondrites: implications for the timing and duration of aqueous alteration. *Geochim. Cosmochim. Acta* **73**, 7433–7442.

de Leuw S., Rubin A. E. and Wasson J. T. (2010) Carbonates in CM chondrites: Complex formational histories and comparison to carbonates in CI chondrites. *Meteorit. Planet. Sci.* **45**, 513–530.

Duke D. A. and Stephens J. D. (1964) Infrared investigation of the olivine group minerals. *Am. Min.* **49**, 1388–1406.

Farmer V. C. (1974) The layer silicates. In *The Infra-Red Spectra of Minerals* (ed. V. C. Farmer). Mineralogical Society, London, pp. 331–364.

Fuchs L. H., Olsen E. and Jensen K. J. (1973) Mineralogy, mineral-chemistry, and composition of the Murchison (C2) meteorite. *Smithsonian Contrib. Earth Sci.* **10**, 39.

Fujiya W., Sugiura N., Hotta H., Ichimura K. and Sano Y. (2012) Evidence for the late formation of hydrous asteroids from young meteoritic carbonates. *Nat. Commun.* **3**, 627.

Garenne A., Beck P., Montes-Hernandez G., Chiriac R., Toche F., Quirico E., Bonal L. and Schmitt B. (2014) The abundance and stability of "water" in type 1 and 2 carbonaceous chondrites (CI, CM and CR). *Geochim. Cosmochim. Acta* **137**, 93–112.

Gradie J. and Tedesco E. (1982) Compositional structure of the asteroid belt. *Science* **216**, 1405–1407.

Greenwood R. C., Burbine T. H., Miller M. F. and Franchi I. A. (2017) Melting and differentiation of early-formed asteroids: The perspective from high precision oxygen isotope studies. *Chemie der Erde-Geochemistry* **77**, 1–43.

Greenwood R. C., Barrat J.-A., Miller M. F., Anand M., Dauphas N., Franchi I. A., Sillard P. and Starkey N. A. (2018) Oxygen isotopic evidence for accretion of Earth's water before a high energy Moon-forming giant impact. *Sci. Adv.* **4**, eaao5928. https://doi.org/10.1126/sciadv.aao5928.

Greenwood R. C., Burbine T. H. and Franchi I. A. (2020) Linking asteroids and meteorites to the primordial planetesimal population. *Geochim. Cosmochim. Acta* **277**, 377–406.

Grimm R. E. and McSween H. Y. (1989) Water and the thermal evolution of carbonaceous chondrite parent bodies. *Icarus* **82**, 244–280.

Grossman L. (1972) Condensation in the primitive solar nebula. *Geochim. Cosmochim. Acta* **38**, 597–619.

Grossman J. N. (1994) The Meteoritical Bulletin, No 76, 1994 January: The U.S Antarctic Meteorite Collection. *Meteoritics* **29**, 100–143.

Haberle C. W. and Garvie L. A. J. (2017) Extraterrestrial formation of oldhamite and portlandite through thermal metamorphism of calcite in the Sutter's Mill carbonaceous chondrite. *Am. Mineral.* **102**, 2415–2421.

Hamilton V. E. (2000) Thermal infrared emission spectroscopy of the pyroxene mineral series. *J. Geophys. Res.* **105**, 9701–9716.

Hamilton V. E. (2010) Thermal infrared (vibrational) spectroscopy of Mg-Fe olivines: a review and applications to determining the composition of planetary surfaces. *Chemie der Erde* **70**, 7–33.

Hamilton V. E. (2018) Spectral classification of ungrouped carbonaceous chondrites I: Data collection and processing. *Lunar Planet. Sci.* **XLIX**, #1759 (abstr.).

Hamilton V. E., Simon A. A., Christensen P. R., Reuter D. C., Clark B. E., Barucci M. A., Bowles N. E., Boynton W. V., Brucato J. R., Cloutis E. A., Connolly H. C., Donaldson Hanna K. L., Emery J. P., Enos H. L., Fornasier S., Haberle C. W., Hanna R. D., Howell E. S., Kaplan H. H., Keller L. P., Lantz C., Li J.-Y., Lim L. F., McCoy T. J., Merlin F., Nolan M. C., Praet A., Rozitis B., Sandford S. A., Schrader D. L., Thomas C. A., Zou X.-D., Lauretta D. S. and OSIRIS-REx Team (2019) Evidence for widespread hydrated minerals on asteroid (101955) Bennu. *Nat. Astron.* **3**, 332–340.

Hanna R. D., Hamilton V. E., Haberle C., King A. J., Abreu N. M. and Friedrich J. M. (2020) Distinguishing relative aqueous alteration and heating among CM chondrites with IR spectroscopy. *Icarus*. https://doi.org/10.1016/j.icarus.2020.113760.

Hanna R. D., Haberle C. W., Hamilton V. E., Lee M. R., King A. J., Lindgren P., Howell E. S., Molaro J. L., Kaplan H. H., Abreu N. M., Friedrich J. M. and Lauretta D. (2019a) Bennu: An aqueously altered and mildly heated CM carbonaceous asteroid. In 82nd Annual Meeting of the Meteoritical Society. #6443 (abstr.).

Hanna R. D., Hamilton V. E., Haberle C. W., Kaplan H. H., Howell E. S., Takir D., Zolensky M. E. and Lauretta D. S. (2019b) What is the hydrated phase on Bennu's surface? Asteroid Science in the Age of Hayabusa2 and OSIRIS-REx. Tucson, AZ. #2029 (abstr.).

Hiroi T., Pieters C. M., Zolensky M. E. and Lipschultz M. E. (1993) Evidence of thermal metamorphism on the C, G, B, and F asteroids. *Science* **261**, 1016–1018.

Hiroi T. and Vilas F. (1995) Characterization of absorption bands (0.6-0.9 μm) in reflectance spectra of primitive asteroids. *Lunar Planet. Sci.* **26**, 611–612.

Hiroi T., Pieters C. M., Zolensky M. E. and Lipschultz M. E. (1996) Thermal metamorphism of the C, G, B, and F asteroids seen from the 0.7 um, 3 um, and UV absorption strengths in comparison with carbonaceous chondrites. *Meteorit. Planet. Sci.* **31**, 321–327.

Howard K. T., Benedix G. K., Bland P. A. and Cressey G. (2009) Modal mineralogy of CM2 chondrites by X-ray diffraction (PSD-XRD). Part 1: Total phyllosilicate abundance and the degree of aqueous alteration. *Geochim. Cosmochim. Acta* **73**, 4576–4589.

Howard K. T., Benedix G. K., Bland P. A. and Cressey G. (2011) Modal mineralogy of CM chondrites by X-ray diffraction (PSD-XRD). Part 2: Degree, nature and settings of aqueous alteration. *Geochim. Cosmochim. Acta* **75**, 2735–2751.

Howard K. T., Alexander C. M. O. D., Schrader D. L. and Dyl K. A. (2015) Classification of hydrous meteorites (CR, CM and C2 ungrouped) by phyllosilicate fraction: PSD-XRD modal mineralogy and planetesimal environments. *Geochim. Cosmochim. Acta* **149**, 206–222.

Ikeda Y. (1992) An overview of the research consortium, Antarctic carbonaceous chondrites with CI affinities, Yamato-86720, Yamato-82162, and Belgica-7904. In Proceedings of the NIPR Symposium on Antarctic Meteorites 5, pp. 49–73.

Ivanova M. A., Taylor L. A., Clayton R. N., Mayeda T. K., NazarovM A., Brandstaetter F. and Kurat G. (2002) Dhofar 225 vs The CM clan: a metamorphosed or new type of carbonaceous chondrite? *Lunar Planet. Sci.* **XXXIII**, #2806 (abstr.).

Ivanova M., Lorenz C. A., Nazarov M. A., Brandstaetter F., Franchi I. A., Moroz L. V., Clayton R. N. and Bychkov A. Y. (2010) Dhofar 25 and Dhofar 735: Relationships to CM2 chondrites and metamorphosed carbonaceous chondrites, Belgica-7904 and Yamato-86720. *Meteorit. Planet. Sci.* **45**, 1108–1123.

Jarosewich E. (1990) Chemical analyses of meteorites: a compilation of stony and iron meteorite analyses. *Meteoritics* **25**, 323–337.

Karunadasaa K. S. P., Manoratnea C. H., Pitawalab H. M. T. G. A. and Rajapaksec R. M. G. (2019) Thermal decomposition of calcium carbonate (calcite polymorph) as examined by in-situ high-temperature X-ray powder diffraction. *J. Phys. Chem. Solids* **134**, 21–28.

Kimura M., Grossman J. N. and Weisberg M. K. (2011) Fe-Ni metal and sulfide minerals in CM chondrites: an indicator for thermal history. *Meteorit. Planet. Sci.* **46**, 431–442.

King A. J., Schofield P. F., Howard K. T. and Russell S. S. (2015a) Modal mineralogy of CI and CI-like chondrites by X-ray diffraction. *Geochim. Cosmochim. Acta* **165**, 148–160.

King A. J., Solomon J. R., Schofield P. F. and Russell S. S. (2015b) Characterising the CI and CI-like carbonaceous chondrites using thermogravimetric analysis and infrared spectroscopy. *Earth, Planets, Space* **67**, 198.

King A. J., Schofield P. F. and Russell S. S. (2017) Type 1 aqueous alteration in CM carbonaceous chondrites: implications for the evolution of water-rich asteroids. *Meteorit. Planet. Sci.* **52**, 1197–1215.

King A. J., Bates H. C., Krietsch D., Busemann H., Clay P. L., Schofield P. F. and Russell S. S. (2019) The Yamato-type (CY) carbonaceous chondrite group: analogues for the surface of asteroid Ryugu? *Geochemistry* **79** 125531.

Kitazato K., Milliken R. E., Iwata T., Abe M., Ohtake M., Matsuura S., Arai T., Nakauchi Y., Nakamura T., Matsuoka M., Senshu H., Hirata N., Hiroi T., Pilorget C., Brunetto R., Poulet F., Riu L., Bibring J.-P., Takir D., Domingue D. L., Vilas F., Barucci M. A., Perna D., Palomba E., Galiano A., Tsumura K., Osawa T., Komatsu M., Nakato A., Arai T., Takato N., Matsunaga T., Takagi Y., Matsumoto K., Kouyama T., Yokota Y., Tatsumi E., Sakatani N., Yamamoto Y., Okada T., Sugita S., Honda R., Morota T., Kameda S., Sawada H., Honda C., Yamada M., Suzuki H., Yoshioka K., Hayakawa M., Ogawa K., Cho Y., Shirai K., Shimaki Y., Hirata N., Yamaguchi A., Ogawa N., Terui F., Yamaguchi T., Takei Y., Saiki T., Nakazawa S., Tanaka S., Yoshikawa M., Watanabe S. and Tsuda Y. (2019) The surface composition of asteroid 162173 Ryugu from Hayabusa2 near-infrared spectroscopy. *Science* **364**, 272–275.

Kullerud G. (1963) Thermal stability of pentlandite. *Can. Mineral.* **7**, 353–366.

Lahfid A., Beyssac O., Deville E., Negro F., Chopin C. and Goffé B. (2010) Evolution of the Raman spectrum of carbonaceous material in low-grade metasediments of the Glarus Alps (Switzerland). *Terra Nova* **22**, 354–360.

Lantz C., Brunetto R., Barucci M. A., Fornasier S., Baklouti D., Bourçois J. and Godard M. (2017) Ion irradiation of carbonaceous chondrites: A new view of space weathering on primitive asteroids. *Icarus* **285**, 43–57.

Lauretta D. S., Hergenrother C. W., Chesley S. R., Leonard J. M., Pelgrift J. Y., Adam C. D., Al Asad M., Antreasian P. G., Ballouz R.-L., Becker K. J., Bennett C. A., Bos B. J., Bottke W. F., Brozović M., Campins H., Connolly H. C., Daly M. G., Davis A. B., de León J., DellaGiustina D. N., Drouet d'Aubigny Y. C., Dworkin J. P., Emery J. P., Farnocchia D., Glavin D. P., Golish D. R., Hartzell C. M., Jacobson R. A., Jawin E. R., Jenniskens P., Kidd J. N., Lessac-Chenen E. J., Li J.-Y., Libourel G., Licandro J., Liounis A. J., Maleszewski C. K., Manzoni C., May B., McCarthy L. K., McMahon J. W., Michel P., Molaro J. L., Moreau M. C., Nelson D. S., Owen W. M., Rizk B., Roper H. L., Rozitis B., Sahr E. M., Scheeres D. J., Seabrook J. A., Selznick S. H., Takahashi Y., Thuillet F., Tricarico P., Vokrouhlický D. and Wolner C. W. V. (2019) Episodes of particle ejection from the surface of the active asteroid (101955) Bennu. *Science* **366**.

Le Corre L., Sanchez J. A., Reddy V., Takir D., Cloutis E. A., Thirouin A., Becker K. J., Li J.-Y., Sugita S. and Tatsumi E. (2018) Ground-based characterization of Hayabusa2 mission target asteroid 162173 Ryugu: constraining mineralogical composition in preparation for spacecraft operations. *Monthly Notices Royal Astron. Soc.* **475**, 614–623.

Lee M. R. (1993) The petrography, mineralogy and origins of calcium sulphate within the Cold Bokkeveld CM carbonaceous chondrite. *Meteoritics* **28**, 53–62.

Lee M. R., Lindgren P., Sofe M. R., Alexander C. M. O. D. and Wang J. (2012) Extended chronologies of aqueous alteration in the CM2 carbonaceous chondrites: evidence from carbonates in Queen Alexandra Range 93005. *Geochim. Cosmochim. Acta* **92**, 148–169.

Lee M. R., Lindgren P. and Sofe M. R. (2014) Aragonite, breunnerite, calcite and dolomite in the CM carbonaceous chondrites: high fidelity recorders of progressive parent body aqueous alteration. *Geochim. Cosmochim. Acta* **144**, 126–156.

Lee M. R. and Lindgren P. (2016) Aqueous alteration of chondrules from the Murchison CM carbonaceous chondrite: replacement, pore filling, and the genesis of polyhedral serpentine. *Meteorit. Planet. Sci.* **51**, 1003–1021.

Lee M. R., Lindgren P., King A. J., Greenwood R. C., Franchi I. A. and Sparkes R. (2016) Elephant Moraine 96029, a very mildly aqueously altered and heated CM carbonaceous chondrite: implications for the drivers of parent body processing. *Geochim. Cosmochim. Acta* **187**, 237–259.

Lee M. R., Cohen B. E., Mark D. F. and Boyce A. (2018) Evidence for widespread post-hydration heating of the CM carbonaceous chondrites. *Lunar Planet. Sci.* **XLIX**, #1285 (abstr.).

Lee M. R., Cohen B. E., King A. J. and Greenwood R. C. (2019a) The diversity of CM carbonaceous chondrite parent bodies explored using Lewis Cliff 85311. *Geochim. Cosmochim. Acta* **264**, 224–244.

Lee M. R., Cohen B. E. and King A. J. (2019b) Alkali-halogen metasomatism of the CM carbonaceous chondrites. *Meteorit. Planet. Sci.* **54**, 3052–3063.

Mayeda T. K. and Clayton R. N. (1998) Oxygen isotope effects in serpentine dehydration. *Lunar Planet. Sci.* **XXIV**, #1405 (abstr.).

McSween H. Y. (1979) Alteration in CM carbonaceous chondrites inferred from modal and chemical variations in matrix. *Geochim. Cosmochim. Acta* **43**, 1761–1770.

Metzler K., Bischoff A. and Stoffler D. (1992) Accretionary dust mantles in CM chondrites: evidence for solar nebula processes. *Geochim. Cosmochim. Acta* **56**, 2873–2897.

Miller M. F., Franchi I. A., Sexton A. S. and Pillinger C. T. (1999) High precision $\Delta^{17}O$ isotope measurements of oxygen from silicates and other oxides: methods and applications. *Rapid Comms Mass Spec.* **13**, 1211–1217.

Mogi K., Yamashita S., Nakamura T., Matsuoka M., Okumura S. and Furukawa Y. (2017) Dehydration process of experimentally heated murchison without any effects of adsorbed and rehydrated water. In 80th Annual Meeting of the Meteoritical Society. #6225 (abstr.).

Molaro J. L., Hergenrother C. W., Chesley S. R., Wash K. J., Hanna R. D., Haberle C. W., Schwartz S. R., Ballouz R.-L., Bottke W. F., Campins H. J. and Lauretta D. S. (2020) Thermal fatigue as a driving mechanism for asteroid activity. J. Geophys. Res. – Planets 125, e2019JE006325. https://doi.org/10.1029/2019JE006325.

Molaro J. L., Walsh K. J., Jawin E. R., Ballouz R.-L., Bennett C. A., Golish D. R., d'Aubigny C. D., DellaGiustina D. N., Rizk B., Schwartz S. R., Delbo M., Hanna R. D., Pajola M., Campins H., Ryan A. J., Bottke W. F. and Lauretta D. S. (2020) In situ evidence of thermally induced rock breakdown widespread on Bennu's surface. Nat. Commun. 11, 2913. https://doi.org/10.1038/s41467-020-16528-7.

Moroz L. V., Schmidt M., Schade U., Hiroi T. and Ivanova M. A. (2006) Synchrotron-based infrared microspectroscopy as a useful tool to study hydration states of meteorite constituents. Meteorit. Planet. Sci 41, 1219–1230.

Nakamura T. (2005) Post-hydration thermal metamorphism of carbonaceous chondrites. J. Mineral. Petrol. Sci. 100, 260–272.

Nakamura T. (2006) Yamato 793321 CM chondrite: dehydrated regolith material of a hydrous asteroid. Earth Planet. Sci. Lett. 242, 26–38.

Nakato A., Nakamura T., Kitajama F. and Noguchi T. (2008) Evaluation of dehydration mechanism during heating of hydrous asteroids based on mineralogical and chemical analysis of naturally and experimentally heated CM chondrites. Earth Planets Space 60, 855–864.

Nazarov M. A., Kurat G., Brandstaetter F., Ntaflos T., Chaussidon M. and Hoppe P. (2009) Phosphorus-bearing sulfides and their associations in CM chondrites. Petrology 17, 101–123.

Nozaki W., Nakamura T. and Nogouchi T. (2006) Bulk mineralogical changes of hydrous micrometeorites during heating in the upper atmosphere at temperatures below 1000 °C. Meteorit. Planet. Sci 41, 1095–1114.

Palmer E. E. and Lauretta D. S. (2011) Aqueous alteration of kamacite in CM chondrites. Meteorit. Planet. Sci. 46, 1587–1607.

Perna D., Barucci M. A., Ishiguro M., Alvarez-Candal A., Kuroda D., Yoshikawa M., Kim M.-J., Fornasier S., Hasegawa S., Roh D.-G., Müller T. G. and Kim Y. (2017) Spectral and rotational properties of near-Earth asteroid (162173) Ryugu, target of the Hayabusa2 sample return mission. Astron. Astrophys. 599(L1), 1–4.

Post J. L. and Borer L. (2000) High-resolution infrared spectra, physical properties, and micromorphology of serpentines. Appl. Clay Sci. 16, 73–85.

Quirico E., Orthous-Daunay F.-R., Beck P., Bonal L., Brunetto R., Dartois E., Pino T., Montagnac G., Rouzaud J.-N., Engrand C. and Duprat J. (2014) Origin of insoluble organic matter in type 1 and 2 chondrites: new clues, new questions. Geochim. Cosmochim. Acta 136, 80–99.

Quirico E., Bonal L., Beck P., Alexander C. M. O. D., Yabuta H., Nakamura T., Nakato A., Flandinet L., Montagnac G., Schmitt-Kopplin P. and Herd C. D. K. (2018) Prevalence and nature of heating processes in CM and C2-ungrouped chondrites as revealed by insoluble organic matter. Geochim. Cosmochim. Acta 241, 17–37.

Remusat L., Derenne S., Robert F. and Knicker H. (2005) New pyrolytic and spectroscopic data on Orgueil and Murchison insoluble organic matter: a different origin than soluble? Geochim. Cosmochim. Acta 69, 3919–3932.

Rubin A. E., Trigo-Rodriguez J. M., Huber H. and Wasson J. T. (2007) Progressive aqueous alteration of CM carbonaceous chondrites. Geochim. Cosmochim. Acta 71, 2361–2382.

Rubin A. E. (2012) Collisional facilitation of aqueous alteration of CM and CV carbonaceous chondrites. Geochim. Cosmochim. Acta 90, 181–194.

Salisbury J. W., Hapke B. and Eastes J. W. (1987) Usefulness of weak bands in midinfrared remote sensing of particulate planetary surfaces. J. Geophys. Res. 92, 702–710.

Salisbury J. W. (1993) Mid-infrared spectroscopy: laboratory data. In Remote Geochemical Analysis: Elemental and Mineraliogical Composition (eds. C. M. Pieters and P. A. J. Englert). Cambridge University Press, New York, pp. 79–98 (Ch. 74).

Sephton M. A. (2002) Organic compounds in carbonaceous meteorites. Nat. Prod. Rep 19, 292–311.

Singerling S. A. and Brearley A. J. (2018) Primary iron sulfides in CM and CR carbonaceous chondrites: Insights into nebular processes. Meteorit. Planet. Sci. 53, 2078–2106.

Sparkes R., Hovius N., Galy A., Kumar R. V. and Liu J. T. (2013) Automated analysis of carbon in powdered geological and environmental samples by Raman spectroscopy. Appl. Spectrosc. 67, 779–788.

Takir D., Emery J. P., McSween J. H. Y., Hibbitts C. A., Clark R. N., Pearson N. and Wang A. (2013) Nature and degree of aqueous alteration in CM and CI carbonaceous chondrites. Meteorit. Planet. Sci. 48, 1618–1637.

Takir D., Stockstill-Cahill K. R., Hibbitts C. A. and Nakauchi Y. (2019) 3-μm reflectance spectroscopy of carbonaceous chondrites under asteroid-like conditions. Icarus 333, 243–251.

Telus M., Alexander C. M. O. D., Hauri E. H. and Wang J. (2019) Calcite and dolomite formation in the CM parent body: Insight from in situ C and O isotope analyses. Geochim. Cosmochim. Acta 260, 275–291.

Tonui E., Zolensky M., Hiroi T., Nakamura T., Lipschutz M., Wang M.-S. and Okudaira K. (2014) Petrographic, chemical and spectroscopic evidence for thermal metamorphism in carbonaceous chondrites I: CI and CM chondrites. Geochim. Cosmochim. Acta 126, 284–306.

Valverde J. M. (2015) On the negative activation energy for limestone calcination at high temperatures nearby equilibrium. Chem. Eng. Sci. 132, 169–177.

Velbel M. A. and Zolensky M. E. (2019) Dehydroxylation and peak temperature of C1 and C2 carbonaceous chondite matrix. Lunar Planet. Sci. L.

Wakita S. and Genda H. (2019) Fates of hydrous materials during planetesimal collisions. Icarus 328, 58–68.

Wilkening L. L. (1978) Carbonaceous chondritic material in the solar system. Die Naturwissenschaften 65, 73–79.

Wopenka B. and Pasteris J. D. (1993) Structural characterization of kerogens to granulite-facies graphite: Applicability of Raman microprobe spectroscopy. American Min. 78, 533–557.

Zolensky M. E. and McSween H. Y. (1988) Aqueous alteration. In Meteoritics and the Early Solar System (eds. J. F. Kerridge and M. S. Matthews). University Arizona Press, Tuscon, pp. 114–143.

Zolensky M. E., Barrett R. and Browning L. (1993) Mineralogy and composition of matrix and chondrule rims in carbonaceous chondrites. Geochim. Cosmochim. Acta 57, 3123–3148.

Zolensky M. E., Mittlefehldt D. W., Lipschutz M. E., Wang M.-S., Clayton R. N., Mayeda T. K., Grady M. N., Pillinger C. and Barber D. (1997) CM chondrites exhibit the complete petrologic range from type 2 to 1. Geochim. Cosmochim. Acta 61, 5099–5115.

Associate editor: Pierre Beck